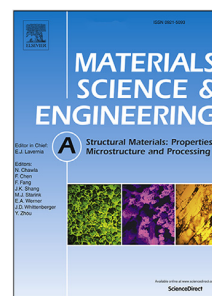# Journal Pre-proof

Dynamic penetration of cellular solids: Experimental investigation using Hopkinson bar and computed tomography

Jan Šleichrt, Tomáš Fíla, Petr Koudelka, Marcel Adorna, Jan Falta, Petr Zlámal, Jonathan Glinz, Michaela Neuhäuserová, Tomáš Doktor, Anja Mauko, Daniel Kytýř, Matej Vesenjak, Isabel Duarte, Zoran Ren, Ondřej Jiroušek

Please cite this article as: J. Šleichrt, T. Fíla, P. Koudelka et al., Dynamic penetration of cellular solids: Experimental investigation using Hopkinson bar and computed tomography, *Materials Science & Engineering A* (2020), doi: https://doi.org/10.1016/j.msea.2020.140096.

This is a PDF file of an article that has undergone enhancements after acceptance, such as the addition of a cover page and metadata, and formatting for readability, but it is not yet the definitive version of record. This version will undergo additional copyediting, typesetting and review before it is published in its final form, but we are providing this version to give early visibility of the article. Please note that, during the production process, errors may be discovered which could affect the content, and all legal disclaimers that apply to the journal pertain.

Highlights

Dynamic penetration of cellular solids: Experimental investigation using Hopkinson bar and computed tomography

Jan Šleichrt,Tomáš Fíla,Petr Koudelka,Marcel Adorna,Jan Falta,Petr Zlámal,Jonathan Glinz,Michaela Neuhäuserová,Tomáš Doktor,Anja Mauko,Daniel Kytýř,Matej Vesenjak,Isabel Duarte,Zoran Ren,Ondřej Jiroušek

- Direct impact Hopkinson bar is used for dynamic penetration of three cellular solids

- Wave separation technique is applied to process Hopkinson bar strain-gauge data

- High-speed camera-based DIC is used to evaluate deformation mode of samples

- Differential XCT allows for advanced volumetric analysis of the microstructural response

- Changes in material behaviour, inertia, and strain-rate effects are investigated

Dynamic penetration of cellular solids: Experimental investigation using Hopkinson bar and computed tomography[★]

Jan Šleichrt[a,*], Tomáš Fíla[a], Petr Koudelka[a,e], Marcel Adorna[a], Jan Falta[a], Petr Zlámal[a,e], Jonathan Glinz[b], Michaela Neuhäuserová[a], Tomáš Doktor[a], Anja Mauko[c], Daniel Kytýř[e], Matej Vesenjak[c], Isabel Duarte[d], Zoran Ren[c] and Ondřej Jiroušek[a]

[a]*Czech Technical University in Prague, Faculty of Transportation Sciences, Konviktská 20, 110 00 Prague, Czech Republic*

[b]*University of Applied Sciences Upper Austria, Stelzhamerstraße 23, 4600 Wels, Austria*

[c]*University of Maribor, Faculty of Mechanical Engineering, Smetanova ul. 17, 2000 Maribor, Slovenia*

[d]*Centre for Mechanical Technology and Automation, Department of Mechanical Engineering, University of Aveiro, 3810-193 Aveiro, Portugal*

[e]*Czech Academy of Sciences, Institute of Theoretical and Applied Mechanics, Prosecká 809/76, 190 00 Prague, Czech Republic*

ARTICLE INFO

ABSTRACT

Light-weight cellular solids, such as aluminium foams, are promising materials for use in ballistic impact mitigation applications for their high specific deformation energy absorption capabilities. In this study, three different types of aluminium alloy based in-house fabricated cellular materials were subjected to dynamic penetration using the in-house experimental setup to evaluate their deformation and microstructural response. Two-sided direct impact Hopkinson bar apparatus instrumented with two high-speed cameras observing the impact area and the penetrated surface of the specimens was used. Advanced wave separation technique was employed to process strain-gauge signals recorded during penetration. Images captured by one of the cameras were processed using an in-house Digital Image Correlation method with sub-pixel precision, that enabled validation of the wave separation results of the strain-gauge signals. The second camera was used to observe the penetration into the tested specimens for correct interpretation of the measured signals with respect to derived mechanical and microstructural properties at different impact velocities. Differential X-ray computed tomography of selected specimens was performed, which allowed for an advanced pre- and post-impact volumetric analysis. Results of performed experiments and elaborate analysis of the measured experimental data are shown in this study.

1. Introduction

Metal foams and other porous solids with similar microstructure are materials suitable for deformation energy mitigation applications due to their low specific density and specific compressive response represented by a typical plateau of constant stress up to very high overall strains yielding their very high specific energy absorption capability [1]. Moreover, cellular materials can be beneficially used as constituents in sandwich structures and composite panels, where the cellular layers are used for dissipation of the kinetic energy of the impacting object, while the other layers maintain the integrity of the panel [2]. However, as cellular materials often have rather complex internal structure, with a significant amount of inhomogeneities, and their deformation mechanisms are complex, design of the protective structures is not a straightforward task. Here, an advanced approach combining an extensive experimental investigation of mechanical characteristics and deformation behaviour with numerical simulations is used [3, 4, 5]. In general, mechanical properties and deformation behaviour of cellular materials are not constant and consistent through-out the whole spectrum of possible loading conditions and scenarios [6]. Energy absorption applications depend on dynamic loading and include dynamic impact, dynamic indentation, penetration, shock or even blast. The effects of strain-rate sensitivity related to inertia effects, layer collapse, strain wave propagation, shock front formation and friction have a fundamental influence on the deformation response of a material [7, 8]. These effects have to be well described, understood, and taken into account during design and optimization phase of the protective device. As the aforementioned effects are very complex and strongly related to specific material, it is not possible to reproduce them easily in numerical simulations using standard material models [9].

*Corresponding author

ORCID(s): 0000-0001-7511-2910 (J. Šleichrt)

Dynamic penetration of cellular solids: Experimental investigation

In recent years, metal foams and other cellular materials have been investigated in a number of research studies covering experimental, numerical and analytical characterization of the material. Under dynamic loading conditions, various types of cellular materials have been tested experimentally using several methods. Drop-weight tests have been used for characterization during low velocity impacts [10]. Hopkinson bar based tests (particularly tests with Split Hopkinson Pressure Bar - SHPB) [11, 12, 13, 14] and Direct impact Hopkinson bar (DIHB) tests [15, 16] have been carried out to investigate the material behaviour at middle to high strain-rates. Taylor anvil test or gas- and powder-gun experiments have been performed to investigate the behaviour during high velocity impacts [17, 18]. A variety of entirely numerical [19] or mixed experimental-numerical studies [20] covering the aforementioned topics have been published. The strain-rate sensitivity [21, 22, 23] and other effects related to dynamic loading such as inertia effects [13, 24], fracture and fatigue behaviour [25, 26, 27], compaction shock [28, 29, 30], wave propagation [31], and cell damage [32] have been investigated in detail. Currently, cellular materials based on artificially manufactured lattice structures [33] and meta-materials [34, 35] are extensively studied. Such studies cover topics including research of non-conventional materials like auxetics (materials with negative Poisson's ratio) [36, 37, 38], inter-penetrating phase composites [39, 40, 41, 42], materials based on an aluminium foam skeleton [43, 44] or their constituents [45].

One of the important dynamic loading modes is penetration or dynamic indentation, where a specimen is impacted with a projectile with cross-section smaller than the cross-section of the specimen. During the test, the projectile penetrates the specimen, while its kinetic energy is dissipated in the material. This mode of loading is fundamental for the description of the crushing under the impacting object as it reliably simulates the conditions during localized impact and can characterize real projectile stopping capabilities of the investigated material. However, the number of published studies is lower than for other loading modes. One of the limiting factors is the complexity of experimental procedures and particularly the instrumentation of the test. Nevertheless, the studies analyzing the localized impact on cellular foams [46], drop-weight based penetration testing of the aluminium foams [47, 48, 49], composite structures, sandwich panels and honeycomb panels [47, 48] are available. The effects of the impactor shape and the localized effects [49, 25, 50, 51, 52] and blast [53, 54] were investigated by several research teams. Moreover, advanced experimental techniques for penetration measurements such as in-situ deceleration analysis have been developed [55]. In general, description of the deformation behaviour of metal foams under impact loading is based on elementary mechanisms such as bending, buckling, and shearing of the cells-walls. While the cells located directly under the projectile are deformed due to bending and buckling, the cells situated alongside the impactor are mainly deformed due to shearing [56]. Based on the observations of deformed specimens of aluminium foam presented in [57], a hemispherical deformation zone caused by a flat-end impactor at velocities in the range $3 - 30\,\mathrm{ms}^{-1}$ is localized directly underneath the impactor. An apparent tear cracking line is spreading ahead of the impactor as the deformation zone is being pushed further into the foam [57].

From the published experimental results it is obvious, that advanced imaging methods have to be applied for a detailed description of the deformation behaviour during penetration. A digital image correlation (DIC) has proved to be particularly suitable for the full-field analysis of the displacement and strain fields in quasi-statics [58] and even in dynamic testing [59, 60, 61]. Application of the state-of-the-art high-speed cameras with DIC has allowed for a complex analysis of the deformation behaviour of cellular [13, 62], lattice structures, auxetics [63], as well as other materials [64] during medium to high-velocity loading.

Based on our experience from previous studies investigating strain-rate sensitivity of cellular materials using the Hopkinson bar with DIC [65, 63, 66, 67], a direct impact Hopkinson bar (DIHB) experimental setup with advanced instrumentation for low to medium velocity penetration of cellular materials has been developed. The setup was designed to overcome problems related to penetration testing. In conventional setups, several limitations negatively affect quality and precision of experimental data or significantly constrain performance reducing the application envelope of the method. Conventional drop-towers can be relatively easily applied for penetration testing [51] and instrumented with sensors such as piezo-electric load-cells. However, the range of available impact velocities is limited by the height of the drop-weight tower. Although methods for increasing maximum impact velocity are available (e.g., spring boosters) the drop-weight method is in general limited to testing with rather low impact velocities. Moreover, common instrumentation of a drop-weight tower using a dynamic load-cell and/or accelerometer does not allow for high precision analysis of dynamic effects in the specimen and often produces noisy signals.

The DIHB is a technique for penetration testing of materials at medium to high strain-rates, where a rigid mass projectile directly impacts a specimen mounted on an instrumented transmission bar (or an anvil). This method is called forward direct impact Hopkinson bar (FDIHB) [68]. For velocities at which wave propagation effects significantly influence the results, a specimen is mounted on a rigid mass projectile and launched towards stationary instrumented

transmission bar. This method is called reverse direct impact Hopkinson bar (RDIHB) [68]. Since both methods are based on the Hopkinson bar techniques and their principle relies on strain waves propagation in elastic slender bars, they produce clean and well-defined signals. However, when the penetration testing is performed on panels or larger specimens, where wave propagation effects cannot be neglected, the RDIHB is seriously limited since the launching of a large specimen or panel against an instrumented transmission bar is challenging or even impossible. Also, the testing is single-sided in principle and complex analysis of the panel behaviour is therefore not possible. To overcome such a problem, a method introducing in-situ deceleration using a stand-alone accelerometer embedded in the impacting projectile [55] has been developed. This very advanced method is based on the DIHB technique and allows for a complex analysis of the behaviour during the penetration. However, the accelerometer usually produces noisy signals that have to be extensively filtered [55]. Application of a Laser Doppler Velocimetry (LDV) to produce high-quality velocity output [69] is also challenging as the sensing pattern has to be located in a relatively large distance from the front face of the projectile that is penetrating the specimen. Incorporation of the wave propagation phenomena into the evaluation procedures is thus not a trivial task.

The mechanical testing can be complemented by radiographic imaging to obtain insight into the deformation mechanism within the microstructure of the investigated specimens. Several advanced experimental methodologies for characterization of the mechanical response of porous solids to loading have been developed recently [70]. A time-resolved XCT (4D XCT) experiments enable to capture the deforming microstructure during the in-situ experiment performed in the CT scanner either in discrete load steps [74], or continuously throughout the loading procedure (so-called on-the-fly CT [71]). The radiographical procedure can be coupled with various processing methods, where attention is focused on digital volume correlation [72] and differential XCT [73]. Using the differential XCT, it is possible to compare the intact specimen before the start of the loading procedure (the reference state) with specimen state at arbitrary load states. This is done by performing various mathematical operations on the reconstructed 3D tomographical images to suppress the common microstructural features and highlight the differences in morphology and topology of the microstructural elements. Such a procedure has already been applied, e.g., in biomechanics to study a microcrack formation in human bones [74] and rock mechanics [75]. Although such methods are usually performed on objects subjected to loading in the quasi-static regime, it is possible to perform the XCT of a dynamically loaded sample by its scanning prior to the loading and after the experiment using an external scanner [76].

In this paper, we introduce a complex experimental setup for the penetration testing of cellular materials based on the Open Hopkinson Pressure Bar (OHPB) [68] method that is instrumented with strain gauges on both sides of the specimen. Wave separation technique is employed to reconstruct the strain-wave histories on the specimen boundaries. High precision force, displacement, and velocity profiles at both sides of the specimen are calculated and analyzed together with the wave propagation phenomenons and dynamic forces equilibrium. The experiments are recorded using a pair of high-speed cameras to enable DIC-based displacement and particle velocity evaluation on both sides of the specimen for verification of the strain-gauge signals together with an optical inspection of the specimen during the penetration. To correctly interpret the results derived from optical and strain-gauge measurements, differential X-ray computed micro-tomography (XCT) is performed to characterize the internal structure of the samples. As a part of the high-resolution XCT procedure, imaging of the intact specimens is used for inspection of the internal structure of all the investigated cellular solids with respect to RVE under the impactor.

The experimental setup is used for penetration testing of three different groups of cellular materials: (i) the closed-cell aluminium alloy foam, (ii) the Advanced Pore Morphology (APM) foam, and (iii) hybrid APM foam (hAPM). As these cellular materials exhibit different deformation behaviour and damage mechanisms during dynamic indentation testing, analysis of characteristic behaviour during low to medium velocity penetration at three different impact velocities in the range $8-18 \text{ ms}^{-1}$ is performed. The penetrated closed-cell metal foam and composite with medium strength matrix specimens are scanned after the impact experiments to obtain 3D images of the loaded state for differential analysis. The differential XCT is then employed to reveal the response of the specimens to medium-rate impact including the localization of deformation around or under the impactor. Based on the complex analysis combining mechanical, optical, and XCT data, the changes in behaviour during penetration together with wave propagation characteristics and damage mechanisms were investigated and the specific trends for each type of the material were formulated.
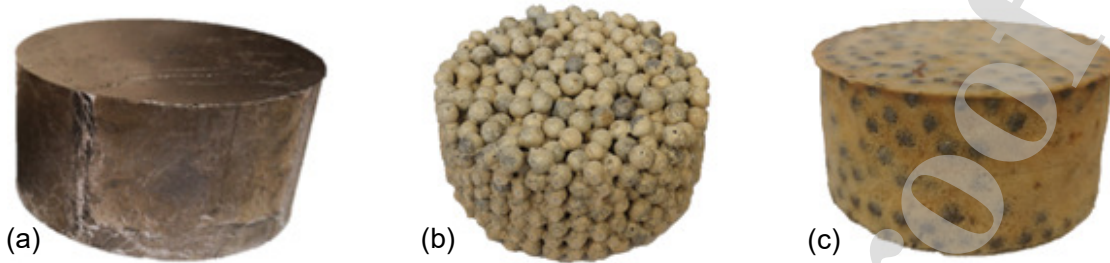
Figure 1: The investigated specimens: (a) the closed-cell aluminium foam, (b) APM, (c) hAPM.

2. Materials and Methods

2.1. Tested materials

Three types of cellular metals were tested: (i) the closed-cell aluminium alloy foam, (ii) the APM foam, where aluminium spheres are coated by polyamide, and (iii) hAPM, where aluminium spheres are embedded in epoxy. A closed-cell aluminium foam with integral metal-skin over the foam core is a typical cellular material for energy absorption applications. Strain-rate sensitivity related to the closed pores and inertia was described in several publications [12, 13, 14, 21, 77]. The wave propagation and shock effects in the pore cells of the metal foam have a crucial influence on the mechanical behaviour [78]. The deformation behaviour of the APM foam, i.e., hollow aluminium spheres composite with non-stiffening matrix, is related mainly to the response of the individual sphere particles and their connectivity, while the binding material maintains the integrity of such a multiphase material. In contrast, the influence of the matrix on resulting deformation behaviour is significant in the hAPM composite, where hollow spheres are embedded in medium strength matrix.

For the production of closed-cell metal foam, a powder-compact foaming technique and a melt route process are mostly used. At the melt route process, a foaming agent or an inert gas are directly injected into a melted metal [79, 80]. For the production of the samples tested in this work, the powder-compact foaming technique was implemented, where the foaming agent was mixed with the metal powder and then compacted to form a foamable precursor material [81, 82, 83]. The precursor was placed into an oven and heated to the temperature close to the melting temperature of its metallic matrix, which allows for the initiation of the foaming process and the consequent expansions of the material.

Closed-cell aluminium alloy ($AlSi_7$) foam samples (diameter of 60 mm; height of 30 mm) were fabricated by applying the the powder-compact foaming technique [81, 82, 83, 84]. Figs. 2(a,b) show reconstructed 3D images of the intact closed-cell alloy foam specimen with the isosurface fitted to cell-struts and identified individual pores colour-coded using their volume. The medial slice captured on the axis of symmetry shows the pore shape variation along with the height of the sample and particularly the morphology of the metal skin. It can be seen that relatively homogeneous pore size distribution was achieved in the central part of the specimen up to approximately half of the specimen height. The pore size then increases with distance from the axis of symmetry and towards the region near the circular face of the cylinder. The variations in external aluminium alloy skin thickness are also apparent. On one face, the thickness of the skin is approximately 0.2 mm, however, on the other face, such thickness can be observed only in the region near the axis of symmetry up to the radius of approximately 10 mm. In the remaining parts of the section, particularly near the vertices, very low-porosity regions were produced during the production process. By inspecting the transversal slices, similar porosity variations have been found also in the circumferential direction.

The fabrication process of the APM aluminium foam ($AlSi_{10}$) samples comprised the foaming and shaping step [81, 85]. Fabrication and coating of the basic APM spheres were done by Fraunhofer IFAM Bremen (Germany). In the second step, the APM specimens were manufactured within the Teflon (PTFE) moulds with a diameter of 60 mm and thickness of 30 mm. The moulds were filled with polyamide coated APM elements and placed into 190 °C heated furnace for two hours to melt the adhesive and to bond together the neighbouring APM elements after cooling. The same manufacturing process was employed for the fabrication of the hAPM foam, which was subjected to heating at 160 °C for three hours. The specimens of the APM and hAPM foam are shown in Fig. 1. Figs. 2(c,d) and Figs. 2(e,f) show reconstructed 3D images of intact APM and hAPM foam specimens. The average densities and weights of the samples are summarized in Tab 1.

Dynamic penetration of cellular solids: Experimental investigation
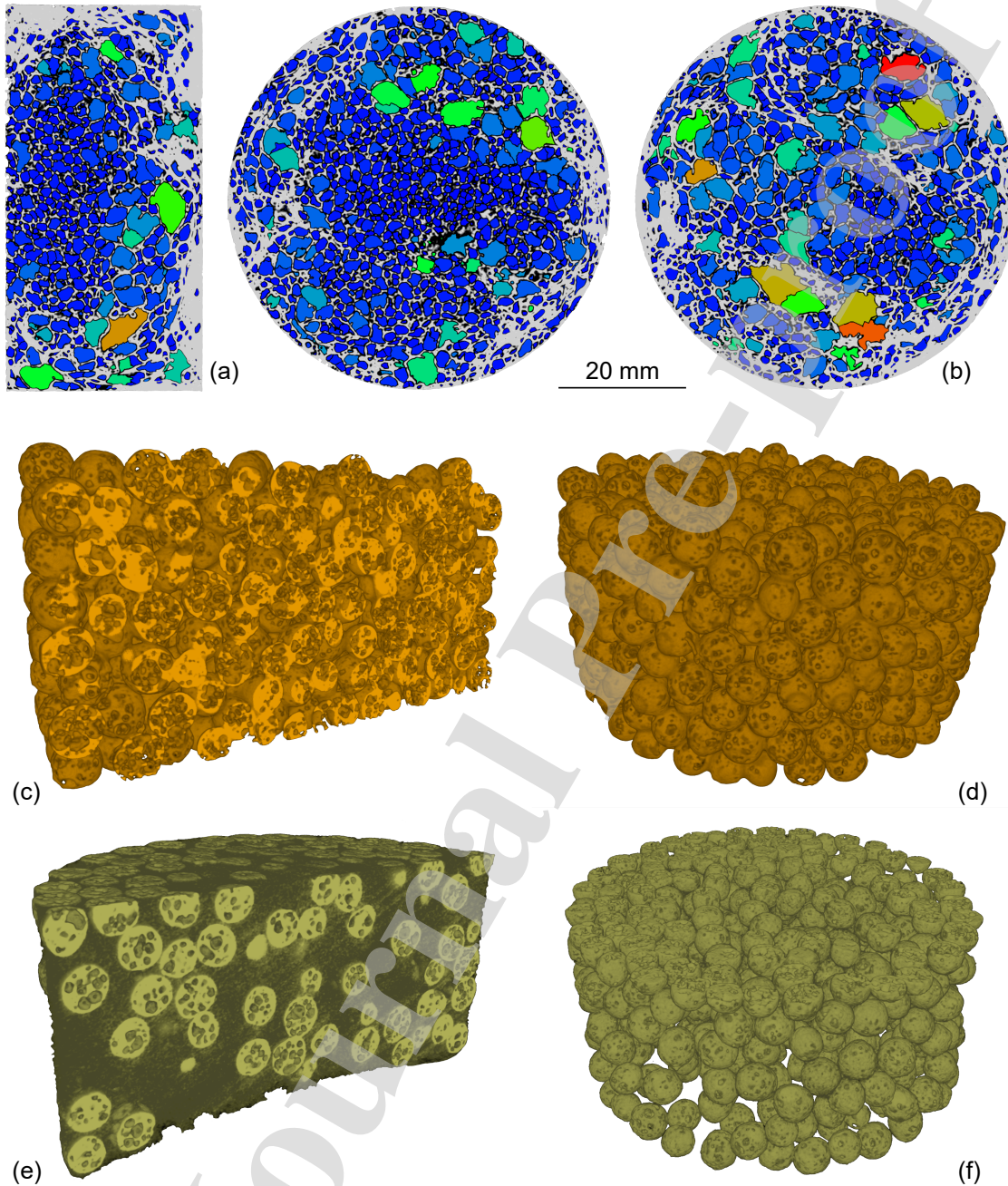
Figure 2: XCT visualisations of investigated materials: closed-cell foam specimen - slice in medial plane (a) and two slices in transversal plane (b); APM and hAPM foam specimens - perspective 3D visualisation using full intensity range (c,e) and segmentation showing only the aluminium spheres (d,f).

The segmentation of the reconstructed 3D images was used to visualise the aluminium spheres and for a general inspection of the sphere morphology as the other structural features were not apparent in the XCT. The visualisation based on full intensity range coupled with sectioning of the volume shows the influence of sphere coating on the resulting internal structure within the cylindrical samples (Fig. 2(d,f)). It can be seen that the APM foam exhibits point-connectivity of spheres yielding approximately 7 spheres along with the height of the sample and 14 spheres in the

Dynamic penetration of cellular solids: Experimental investigation

Table 1
The morphological properties of the specimens

	closed-cell aluminium foam	APM foam	hAPM foam
Density average [kg · m^{-3}]	742.41 ± 47.53	597.03 ± 18.28	525.43 ± 15.40
Weight average [g]	61.73 ± 4.94	51.81 ± 1.66	44.29 ± 1.35

Figure 3: Principle of the direct impact Hopkinson bar methods.

radial direction. The analogous section in the 3D image of hAPM specimen shows significantly different microstructure, where the spheres are predominantly distributed in the region of one circular face and along the circumferential direction near the surface of the specimen. The volume around the axis of symmetry is then composed of approximately 50 % of epoxy matrix and 50 % of aluminium spheres, which is an important finding influencing the interpretation of penetration results with regard to conclusions on material properties. Overall, it can be observed that the requirements on the RVE dimensions, as defined by Gibson and Ashby for porous solids in [1], are fulfilled for all samples when considering the flat-face impactor with diameter 20 mm used in experimental investigation.

2.2. Mechanical testing

Open Hopkinson Pressure Bar (OHPB) is a novel DIHB introduced in 2016 by Govender et al. [68]. The method combines the arrangements of the forward and reverse DIHB (FDIHB, RDIHB). Because the FDIHB cannot capture the phenomenons related to wave propagation and shock front at the front face of the specimen, the RDIHB has to be employed for such measurements. Using this method, the specimen is launched together with a striker towards the transmission bar, where its response is recorded. Since the method is instrumented on a single side only, additional instrumentation is required for measurement of displacements during the experiment (e.g., DIC or LDV) to evaluate displacement, velocity, and force histories at both sides of the specimen.

In our case, the OHPB experimental setup was modified for penetration testing. The experiments were observed with a pair of high-speed cameras to enable optical inspection of the experiments and subsequent processing using DIC. As a standard experiment duration is limited to a relatively short time window (like other variants of Hopkinson bar methods) before the forward and backward propagating strain waves produce superposition at the strain-gauge, the experiment duration was prolonged by applying the wave separation technique verified using information from DIC.

The samples were penetrated by an aluminium alloy bar at three different impact velocities to evaluate the response of tested materials to dynamic loading and to reveal a possible strain-rate sensitivity or inertia effects, wave propagation, and shock related changes in the deformation behaviour. The incident bar was accelerated using a single-stage gas-gun with a maximum operating pressure of 1 MPa and used as a striker that directly penetrated the samples. Tested specimens were placed on a support plate with dimensions corresponding to the sample which was firmly mounted at the end of the transmission bar, see Fig. 3.

The device consisted of aluminium bars made of high-strength aluminium alloy (EN-AW-7075-T6) with a diameter of 20 mm. The incident bar had a length of 1600 mm. The bar was in its front part guided by a linear guideway (drylinT, Igus, USA). The maximum impact velocity of approximately 20 ms^{-1} corresponding to the impact energy of approximately 300 J could be achieved. The transmission bar had a length of 1600 mm. Specimen's supporting plate with a diameter of 60 mm and thickness of 40 mm was connected to the transmission bar using a bolted joint. An additional bar with a length of 1600 mm, serving as momentum and strain-wave trap, was mounted behind the transmission bar. The residual energy of the experiment was dissipated in the momentum trap and a hydro-pneumatic damper. To measure the strain waves propagating in the setup, the incident and transmission bars were instrumented with foil strain-gauges (3/120 LY61, HMB, Germany). A pair of strain-gauges was placed in a distance of 200 mm from the

Dynamic penetration of cellular solids: Experimental investigation
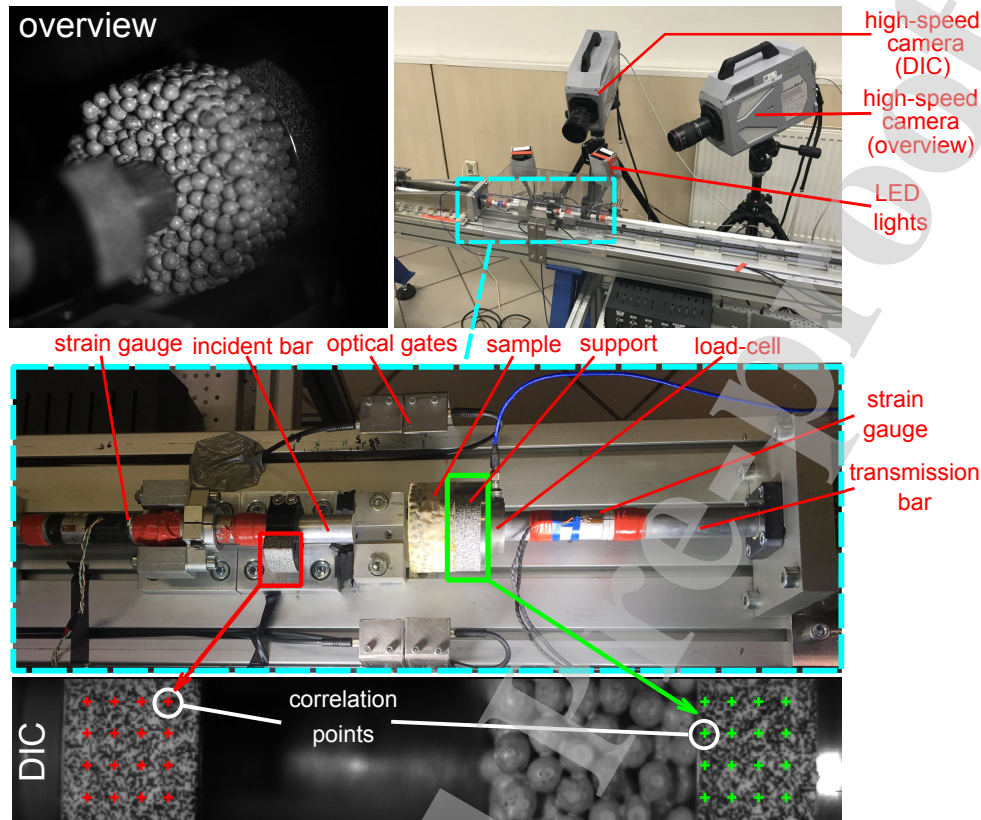
Figure 4: The OHPB experimental setup: High-speed cameras, their field of view and an example of the grid of correlation points established in the incident and transmission bar.

specimen on both adjacent bars and connected in a Wheatstone half-bridge arrangement, so that any possible minor bending of the bars during the experiment was compensated. Moreover, the signal amplification was doubled in comparison with a single strain-gauge connected in a quarter-bridge arrangement. The strain-gauge signals were amplified using a pair of differential low-noise amplifiers (EL-LNA-2, Elsys AG, Switzerland). The signals were recorded with a high-speed digitizing card (PCI-9826H, ADLINK Tech., Taiwan) at a sampling rate of 20 MHz. Photoelectric sensors (FS / FE 10-RL-PS-E4, Sensopart, Germany), serving as an optical gate, were placed in front of the tested sample perpendicularly to the incident bar trajectory and were used for triggering and time synchronization of the experiment. A pair of high-speed cameras (Fastcam SA-Z, Photron, Japan) was used for optical inspection of the experiment. The first camera (called an overview camera in the further text) served for an inspection of the specimen's front face during the impact. It was set to a recording speed of 20 kfps and a resolution of 1024×1024 pixels. The second camera (called DIC camera in the further text) was oriented perpendicularly to the setup's longitudinal axis and observed the ends of both bars, where random speckle patterns were mounted. It was operated at a frame rate of 180 kfps and a resolution of 768×112 pixels. Images from this camera were subsequently processed using the in-house DIC tool [86] for: (i) identification of the displacements of the individual bars, (ii) precise calculation of initial impact velocity, and (iii) identification of longitudinal strain on the surface of the penetrated specimens, when possible. Illumination of the scene was performed using a high-performance LED illumination system (Multiled QT, GS Vitec, Germany). Both cameras were synchronized with the aforementioned photoelectric sensors and with high-speed digitizers. Data acquisition and control during the experiment were performed using a custom LabView (National Instruments, USA) interface. The experimental setup is shown in Fig. 4.

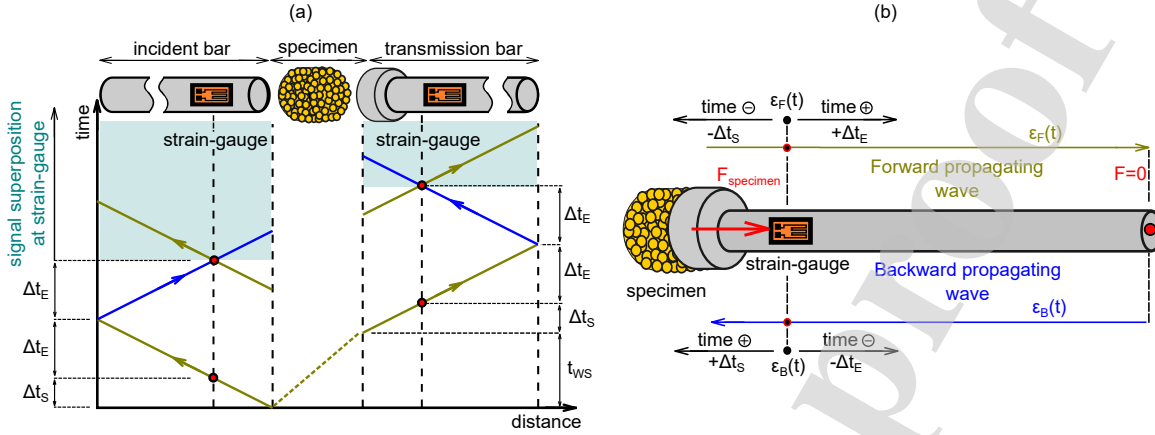Dynamic penetration of cellular solids: Experimental investigation

Figure 5: Lagrange wave propagation diagram in the OHPB experiment.

2.3. Wave separation and data processing

Strain-gauge signals can be used for evaluation of particle velocity, displacement and force at the boundaries of the specimen. In the standard OHPB experiment, calculation of these quantities is based on the one-dimensional strain-wave propagation theory in elastic slender bars [87, 68]. This theory is valid only in a relatively short period of time, when the recorded strain-gauge signals are not affected by backwards-propagating strain-wave that is reflected from the free end of the bar. When the reflected strain-wave arrives at the strain-gauge location, the superposed signal is measured and it cannot be directly used for the evaluation of the mechanical results. Lagrange diagram of wave propagation in the OHPB experiment is shown in Fig. 5. It can be seen that the strain-wave travels from the specimen's boundary through the free end, when it is reflected. The wave travel time required for the distance from the bar face to the location of the strain-gauge is denoted Δt_s. The wave travel time required for the distance from the strain-gauge location to the free end of the bar is denoted Δt_e. The wave superposition occurs, when the reflected wave arrives at the location of the strain-gauge. In our case, this occurs after the time period of $2\Delta t_\mathrm{e}$ after the wave is detected by the strain-gauge for the first time.

As the initial strain-wave propagates always from the specimen in case of OHPB, a wave separation technique can be employed to prolong the experimental time window. Methods for wave separation in Hopkinson bar experiments have been established and can be used for elastic as well as visco-elastic bars [88, 89, 90]. The main assumption of all the methods is that the measured signal $\epsilon(t)$, particle velocity $v(t)$, and the actual force at a certain cross-section $F(t)$ of the bar are given by [89]

$$\epsilon(t) = \epsilon_\mathrm{F}(t) - \epsilon_\mathrm{B}(t), \tag{1}$$
$$v(t) = c_0\left[\epsilon_\mathrm{F}(t) - \epsilon_\mathrm{B}(t)\right], \tag{2}$$
$$F(t) = EA\left[\epsilon_\mathrm{F}(t) + \epsilon_\mathrm{B}(t)\right], \tag{3}$$

where $\epsilon_\mathrm{F}(t)$ is the forward-propagating strain-wave, $\epsilon_\mathrm{B}(t)$ is the backward-propagating strain-wave and c_0 is the wave propagation velocity in the bars. Normally, at least two strain-gauge locations are required on a single bar to reconstruct the forward and backward propagating waves from the measured signals using different techniques [89]. The wave dispersion effects and attenuation have to be taken into account [91, 92, 88, 89, 90]. However, in case of OHPB testing of cellular materials, some simplifications can be adopted that significantly reduce the complexity of the wave separation procedure. Here, the following conditions are met:

- Waves travel from the specimen's boundary to the free end of the bar.

- Waves are generated directly by the bar-specimen contact and the specimen has the lowest mechanical impedance in the experimental setup.

Dynamic penetration of cellular solids: Experimental investigation
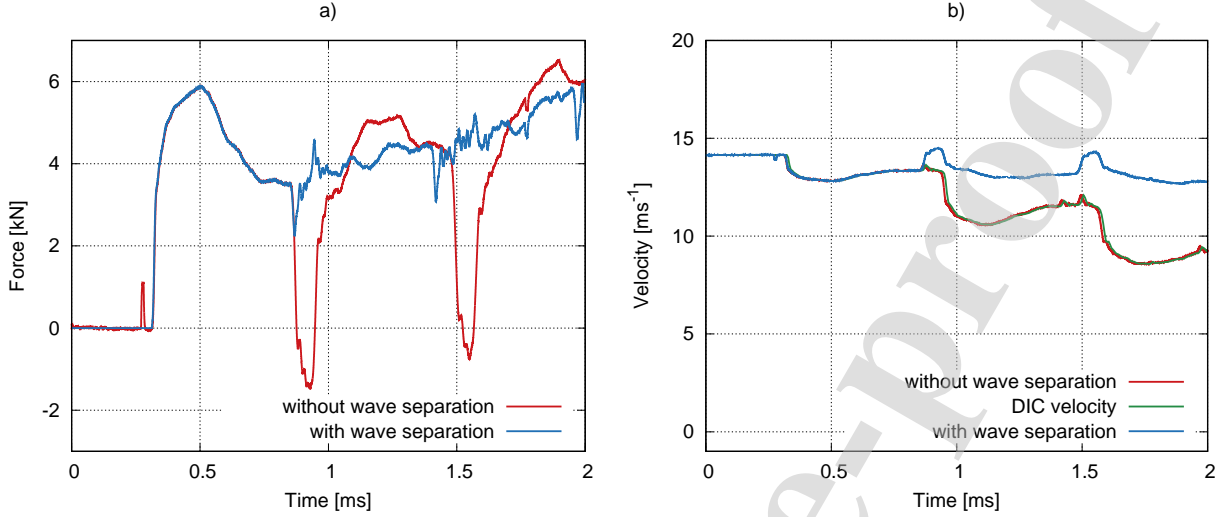
Figure 6: (a) Incident bar force indicated by strain-gauge calculated without wave separation (blue) and with wave separation (red). (b) Incident bar velocity indicated by strain-gauge calculated without wave separation (blue), with wave separation (red) and compared with velocities calculated using DIC (green).

- Wavelength of the strain pulses is very long, while high frequencies are not present in the pulse as they are filtered by the plastic deformation of the specimen. Therefore, wave attenuation and dispersion effects can be considered negligible.

By applying the time-shifting procedure shown in Fig. 5b, the forward and backward propagating waves and other respected quantities at the specimen's location can be calculated using the equations

$$\epsilon_{\text{FS}}(t - \Delta t_{\text{s}}) = \epsilon(t) + \epsilon_{\text{F}}(t - 2\Delta t_{\text{e}}), \tag{4}$$

$$\epsilon_{\text{BS}}(t - \Delta t_{\text{s}}) = -\epsilon_{\text{F}}(t - 2\Delta t_{\text{e}} + \Delta t_{\text{s}}), \tag{5}$$

$$v(t - \Delta t_{\text{s}}) = c_0 \left[\epsilon_{\text{FS}}(t - \Delta t_{\text{s}}) - \epsilon_{\text{BS}}(t - \Delta t_{\text{s}}) \right], \tag{6}$$

$$F(t - \Delta t_{\text{s}}) = EA \left[\epsilon_{\text{FS}}(t - \Delta t_{\text{s}}) + \epsilon_{\text{BS}}(t - \Delta t_{\text{s}}) \right]. \tag{7}$$

Since the wave dispersion effects are considered negligible in case of cellular materials penetration, the separated signals can be calculated using the simple time-shifting procedure that does not change the shape nor amplitude of the wave over the travelled distance. Note that at the beginning of the experiment, the strain-gauge signal $\epsilon(t)$ is never superposed. Therefore, it is possible to separate the waves using the information from the initial time window without superposition.

The wave separation technique allows for evaluation of the experiment in a longer time window when the superposed signal is measured by strain-gauges. The comparison of the force calculated directly from the superposed strain-gauge signal at the incident bar and the force calculated using the wave separation technique is shown in Fig. 6a. The sudden drops in the superposed signal are caused by the backwards-propagating wave. A similar comparison of velocity calculated directly from the superposed signal and the velocity calculated using the wave separation procedure is shown in Fig. 6b.

Displacement calculated from the strain-gauge can be time-shifted to the location of the random speckle pattern and compared with the DIC displacement. If a sufficient number of images with reliable tracking by DIC is available, particle velocity can be calculated by differentiation of the DIC displacement and compared with the value evaluated based on the strain-gauge measurement.

Dynamic penetration of cellular solids: Experimental investigation

2.4. Differential CT procedure

Using the reconstructed 3D images of the intact and impacted samples, differential tomography procedure was performed to emphasize variations within the sample microstructure and to suppress common features in the microstructure with the concentration on the region in the vicinity of the impacting bar. Due to the nature of dynamic loading and the used experimental setup, it was not possible to perform the tomographic scanning using the in-situ methodology. Thus, careful separation of the reconstructed volumes from the scanned stack of samples and their precise subsequent alignment was required to obtain relevant data for morphological analysis. For the alignment of the volumes, a 3D image registration algorithm based on a rigid transformation (i.e., transformation considering only the translations and rotations of the sample yielding 6 degrees of freedom for the registered 3D image) with single-voxel precision was carried out in the VGStudio MAX 3.3 (Volume Graphics, Germany).

After the alignment of the volumes, two approaches for the differential tomography were used in the processing and visualisation of the data. The reference 3D image of the intact specimen was subtracted from the 3D image of the impacted sample. Additionally, blended volumes were created. The blending procedure consists of multiplication of the volume in the impacted state by a given constant followed by a sum of such a volume with the volume of the reference state. This procedure is common for 4D XCT, where such an approach can be used for, e.g., investigation of fatigue microcracks in bones (see [74]). The value of the constant for the multiplication can be obtained from an iterative procedure, where the resulting blended volume is qualitatively inspected for noise and contrast on the boundary of the region influenced by the impact to identify the optimum value. The value of multiplier was sought in the range of $m \in \langle 2; 20 \rangle$, $m \in \mathbb{Z}$, yielding the optimal value of $m = 5$ for the closed-cell foam sample and $m = 10$ for the hAPM foam sample used in the volumetric blending of the reconstructed 3D images. After the differential tomography procedure, the generated volumes were subjected to defect (both the closed-cell foam and the hAPM foam samples) and foam structure analysis (only the closed-cell foam sample). Using the foam structure analysis, the pore morphology in terms of pore-size distribution and strut-/wall-thickness analysis was extracted from the 3D images using the *Foam analysis module* of the VGStudio MAX 3.3 software together with the visualisation of the individual pores and the strut thicknesses. The foam structure analysis module was then used to identify individual cells including their morphological properties for further analysis.

2.5. Experiments

The OHPB experimental setup was used to penetrate the specimens during low and medium velocity impact. The specimens were mounted on the supporting plate attached to the transmission bar. During the mounting, a small amount of grease was applied on the rear face of the specimen to hold the specimen on the plate by friction. The specimens were penetrated using the flat-face incident bar projectile with a total mass of approximately 1.5 kg. The gas-gun air reservoir pressure of 200 kPa, 500 kPa, and 800 kPa was used to accelerate the incident bar to impact velocities of approximately 8 ms^{-1}, 14 ms^{-1} and 18 ms^{-1}. The momentum trap system was not in initial contact with the bars of the experimental setup. This configuration was employed to prevent the subsequent hard impacts on the specimen after the first impact. It also prevented an unknown reflection of the wave on the rear face of the transmission bar, and, therefore, it was used for conservation of the waves in the experimental setup and reconstruction of the wave propagation in the system. In our case, employing a very long transmission bar preventing the arrival of the reflected wave prior to the end of the experiment was not possible due to space limitations. When the accelerated incident bar interrupted the first optical gate in front of the specimen, the data acquisition system and both high-speed cameras were triggered. All the data were automatically uploaded to the control PC after the experiment.

3. Results

The experimental data were processed using the data processing methods described in Section 2. It was possible to evaluate force, displacement, and velocity-time histories that were synchronized with the DIC results and with the images captured by the overview camera. The processed strain-gauge data were compared with the DIC data in terms of indicated displacements and velocities and the output of the wave separation procedure was verified. Thus, it was possible to evaluate all the penetrations until the end of the experiment, i.e. when impact velocity decreased to zero. As the experiments were carried out without any initial contact between the transmission bar and the momentum trap, not all initial kinetic energy was dissipated in the specimen. A part of the initial energy of the incident bar was dissipated in the specimen, while the rest was transformed to the post-impact movement of the bars or dissipated as friction and other losses in the system. This arrangement allowed for analysing the effects related to the wave propagation

Dynamic penetration of cellular solids: Experimental investigation

(a)

(b)

(c)
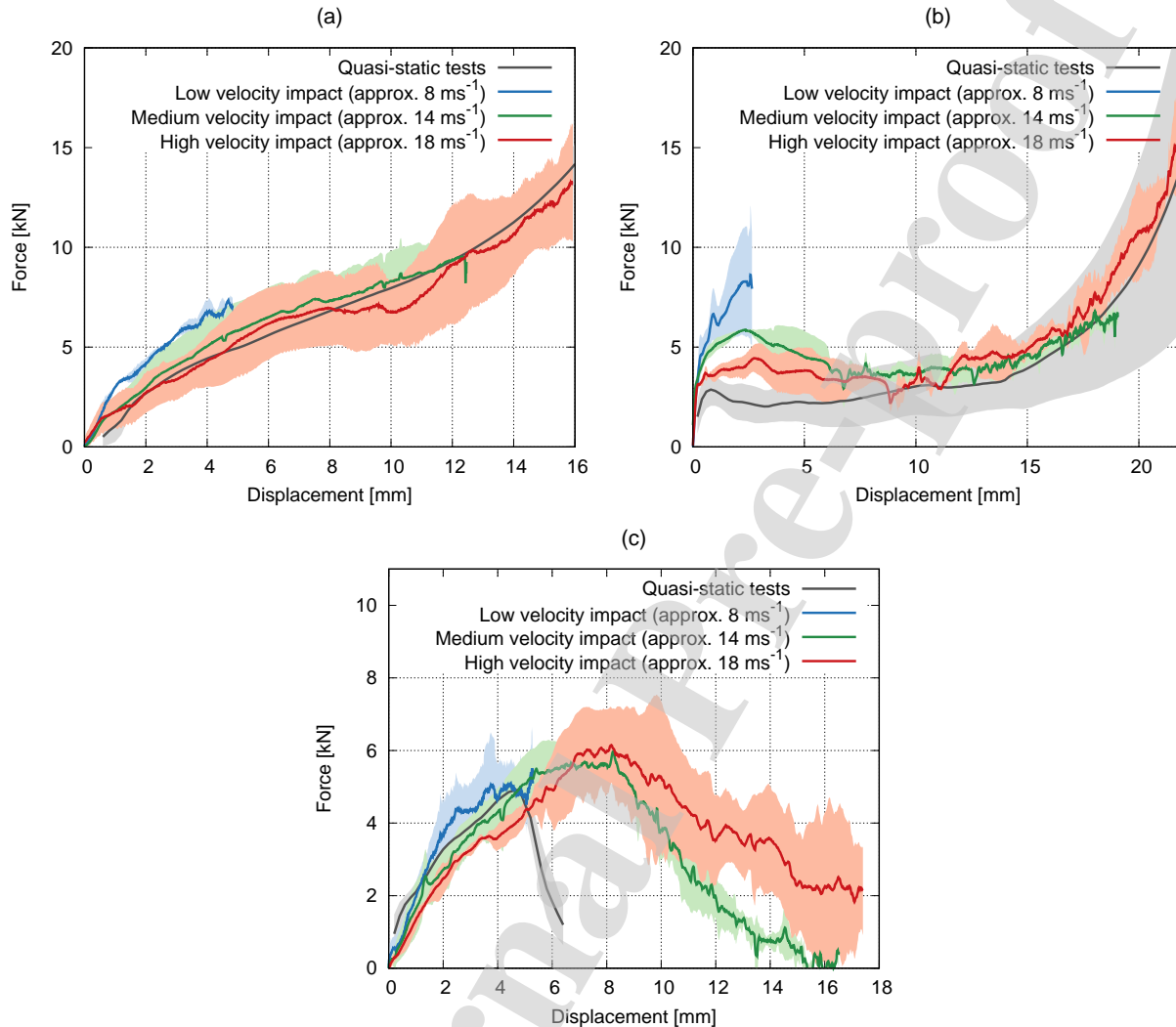
Figure 7: The average force-displacement diagrams for quasi-static and dynamic indentation at three impact velocities: (a) the closed-cell aluminium foam (b) the hAPM foam, (c) the APM foam.

in the specimen. In this section, results evaluated from the strain-gauges including force, displacement, velocity, or energy during the impact are presented and compared with the optical and DIC data. Results regarding a pre-impact as well as a post-impact analysis of the specimen's internal structure are also provided and discussed. At least three specimens were tested in quasi-static compression and dynamic penetration at each impact velocity. However, it has to be mentioned that in some experiments the measured values deviated from the average values of the set. Therefore, the exact values of the material properties had to be interpreted with caution. Still, the trends in the deformation behaviour could be observed, evaluated and discussed. From each type of the tested materials, only one specimen could be processed using the XCT analysis because of its complexity, time-consuming measurements and data processing.

3.1. Force-displacement

The dependency of the piercing force on penetration depth was evaluated. Quasi-static penetration experiments with an identical configuration of the specimen, supports, and indenter were also carried out (see Section A.1).

Force-displacement diagrams of the closed-cell aluminium foam for quasi-static and dynamic indentation at all the impact velocities are shown in Fig. 7a. The closed-cell aluminium foam penetrated at the low impact velocity exhibited

Dynamic penetration of cellular solids: Experimental investigation

behaviour that is not typical for such material as long as the piercing force increased abruptly and no plateau region was observed. Simultaneously, the penetration depth was very low and, in most of the cases, the metal skin over the porous core was not fully penetrated. During the impact at the medium velocity, the behaviour of the specimen was different. In this case, the initial increase of the piercing force is not as significant as in the low-velocity case and, after the initial penetration phase, plateau region typical for foam material was observed. During the high-velocity impact, the behaviour of the specimen was similar to its response on quasi-static indentation, while the average values of piercing force at plateau were higher. The corresponding average force-displacement diagrams of the hAPM foam are shown in Fig. 7b, where monotonous hardening with penetration depth at all the tested impact velocities can be observed. While the specimens remained compact for the low and medium impact velocity, the disintegration of the specimens occurred in the experiments with the high impact velocity. Similarly to the closed-cell aluminium foam, the piercing force decreased with the increasing impact velocity. In this case, the trend was much less profound than in case of the closed-cell foam and standard-deviations for the individual impact velocities partially overlap.

The average force-displacement diagrams of the APM foam are shown in Fig. 7c. The APM foam exhibited similar behaviour to hAPM foam as a monotonous hardening with the penetration depth at all the tested impact velocities was observed. Specimens of this material always disintegrated at medium and high impact velocity. At low impact velocity, most of the specimens remained compact. In one case, the disintegration occurred at approximately identical force and depth as in the quasi-static penetration tests. As in the case of the hAPM foam, the piercing force decreased with the increasing impact velocity. For this material, the effect is even less profound than in the previous case and, again, standard deviations for the individual impact velocities partially overlap.

3.2. Velocity-time

The diagrams showing the change of the actual impact velocity in time were evaluated to investigate the stopping capabilities of the individual materials are shown in Fig. 8. The average time-velocity histories for each type of material at every impact velocity are presented. The velocities were evaluated from strain-gauges as well as from DIC. In all the experiments, a very good agreement of the DIC indicated displacements (or velocities) with the strain-gauges data was observed.

The time-velocity histories of the closed-cell aluminium foam for every impact velocity are shown in Fig. 8a. The closed-cell aluminium foam was able to stop the projectile without any disintegration in all conducted experiments. For this type of material, significant step-wise changes in the impact velocity were observed. This phenomenon was caused by the nature of the testing based on the wave propagation as the relatively long bar was used for penetration of the specimen. The step-wise change occurred every time, when the reflected wave from the free end of the bar arrived at the specimen and caused a sudden change in the velocity. This behaviour was most profound for the case of the closed-cell aluminium foam as the wave generated at the plateau region was approximately constant. Then, the backwards-propagating reflected wave had a similar amplitude with the forward-propagating wave still generated at the plateau. At the high impact velocity, rapid deceleration of the projectile was observed as the penetrated region was compressed to full densification. Here, the projectile was stopped even sooner than at the medium velocity.

The time-velocity histories of the hAPM foam for every impact velocity are shown in Fig. 8b, where a different velocity-time relationship can be observed. The velocity change was rather smooth and continuous. Even though the disintegration of the specimens was observed at the high impact velocity, all the specimens were able to reach zero impact velocity. The disintegration always occurred at the very end of the experiment.

The time-velocity histories of the APM foam for impact velocities are shown in Fig. 8c. The APM foam exhibited a very different behaviour to the other materials. The stopping capability of this material was very low as the specimens disintegrated at both the medium and the high-velocity impacts and allowed the projectile to penetrate through. The decelerated velocity prior to the disintegration was in the order of a few metres per second (lower than $4\,\mathrm{ms}^{-1}$).

3.3. Energy absorption

The energy absorption properties were evaluated to further investigate the stopping capabilities of the individual materials. Also, specific energy absorption ratio defined as the energy dissipated per a unit of nominal penetrated volume was calculated. The diagram showing the energy dissipated per penetration volume for all three materials is shown in Fig. 9a.

The closed-cell foam exhibited the highest value from all the materials at the low impact velocity. For the medium velocity, its energy absorption per volume dropped by approximately 30 % and again increased at the high impact velocity. This behaviour was in agreement with the presented average force-displacement diagrams. Very high energy

Dynamic penetration of cellular solids: Experimental investigation
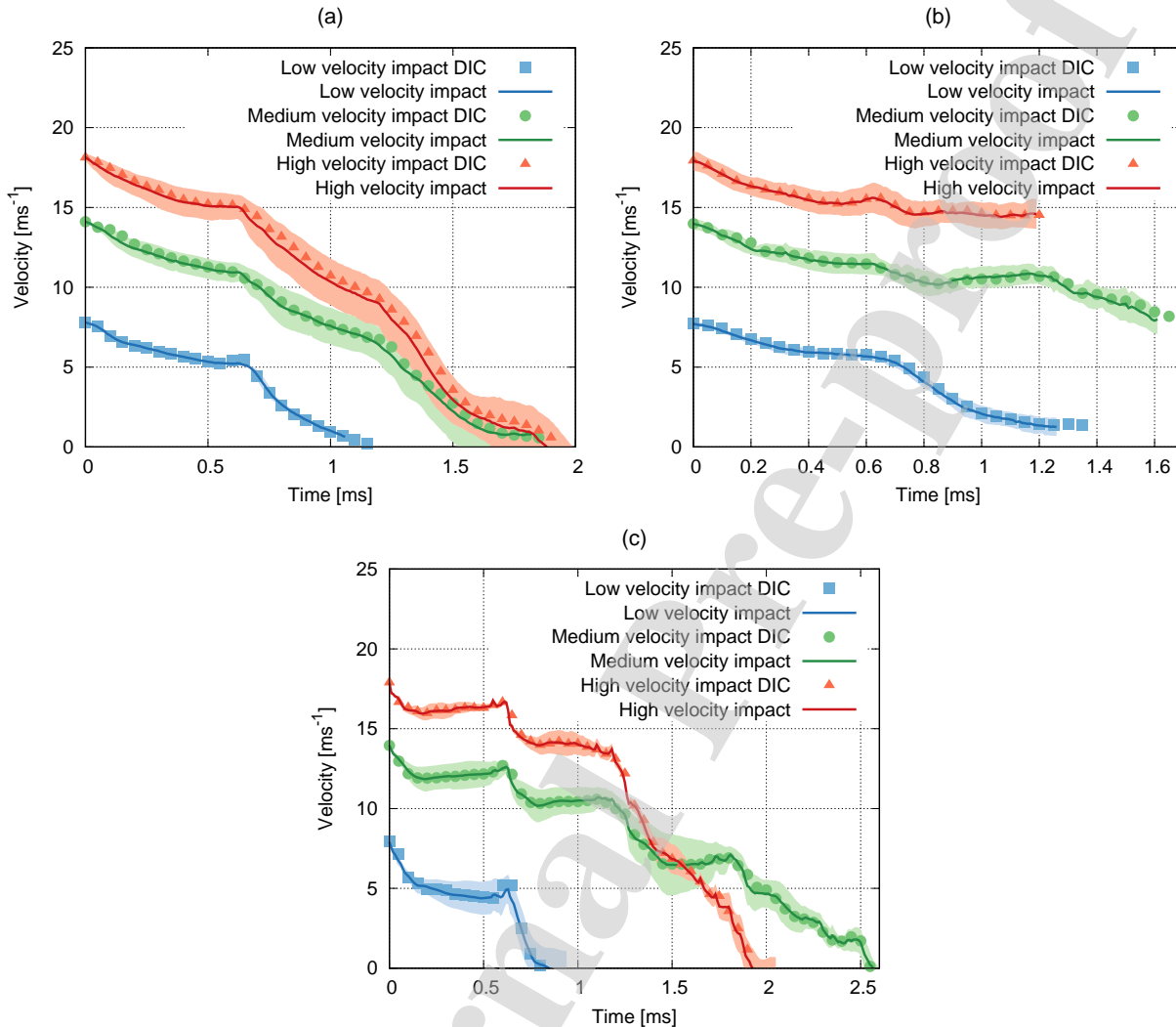
Figure 8: The average velocity-time diagrams for three initial impact velocities showing velocity indicated by the strain-gauges and by the DIC: (a) the closed-cell foam, (b) the hAPM foam, (c) the APM foam.

absorption at the low velocity is related to the crushing behaviour, where the metal skin over the porous core had a significant effect on the wave propagation characteristics and resulted in the corresponding hardening. The effect is discussed in detail in the section related to the specific results of the closed-cell aluminium foam (see Section 3.5.1). The hAPM foam exhibited a monotonous increase of the energy dissipated per volume through all the impact velocities, whereas the APM foam exhibited the inverse trend. In the case of hAPM foam, the energy dissipated per volume monotonically decreased with the impact velocity. The decrease of energy absorption of the APM foam was related to its disintegration at higher velocities. Conversely, the increase of the energy absorption of the hAPM foam was related to its monotonically increasing force-displacement response.

At a penetration depth of 3.5 mm, Fig. 9b shows a stable decrease in energy absorption for all the materials in the initial phase of the impact. Furthermore, similar effects in wave propagation through the specimen related to the impact velocity are visible.

A ratio between the energy dissipated in the specimen and the initial impact energy was calculated to compare the amount of energy dissipated in the material. At the low impact velocity, the ratio was almost identical for all the materials. This behaviour was related to the fact that all three materials were able to withstand the impact at such a low

Dynamic penetration of cellular solids: Experimental investigation
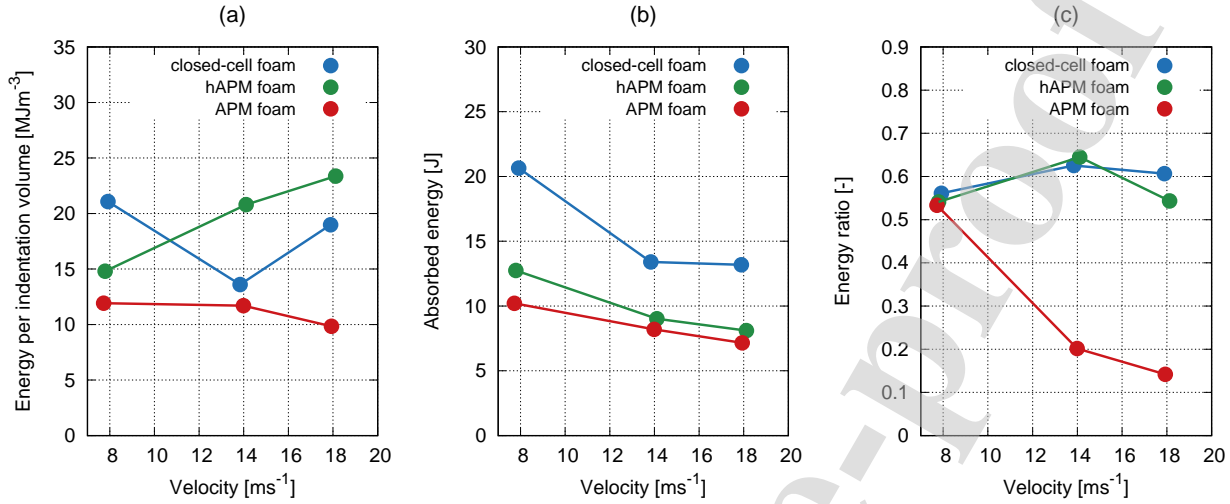
Figure 9: (a) The diagram showing the energy dissipated per penetration volume for all three materials. (b) The diagram showing the energy dissipated per penetration volume for all three materials in the penetration depth of 3.5 mm representing the initial phase of the impact. (c) The ratio of the energy dissipated in the specimen and the initial kinetic energy of the incident bar.

velocity and the residual energy was transferred into the transmission bar through the specimen. With the increasing velocity, the ratio for the APM foam rapidly decreased as it was not able to withstand the impact and disintegrated. On the other hand, the closed-cell foam, as well as the hAPM foam, exhibited similar increased values for the impact at the medium velocity since both materials were able to withstand the impact. At the high impact velocity, the hAPM material lost its ability to withstand the impact (disintegration occurred in the later phase of the impact) and exhibited lower values than the closed-cell foam that remained compact in all the experiments. The ratio of the energy dissipated in the specimen and the impact energy is shown in Fig. 9c.

Because it was not possible to perform the differential CT procedure for the APM foam as the penetration of all the specimens in this group disintegrated at the medium and high-velocity impact. The dependency of the penetration depth, where the disintegration occurred, plotted against the initial impact velocity is shown in Fig.10a. Time, when the disintegration of the specimen started, plotted against the initial impact velocity is shown in Fig.10b. Note that the penetration depth of disintegration increased with the impact velocity, whereas the time of disintegration remained approximately constant. Therefore, the inertia effects delayed the disintegration of the specimen with the increasing impact velocity and this type of material could not withstand even the lower impact energy corresponding with the medium impact velocity. The observed increase in the penetration depth did not represent an increase in energy absorption, but it is only related to the time that is necessary to overcome the inertia and to disintegrate the specimen.

3.4. Wave propagation velocity and dynamic forces equilibrium

Wave propagation velocity and convergence of dynamic forces at both faces of the specimen were analyzed to investigate possible differences that could be attributed to the wave propagation and mechanical impedance of the material. Two parameters were evaluated: (i) wave propagation time through the specimen, (ii) time of the specific convergence of the dynamic forces. The wave propagation time was calculated as the delay between the detection of the incident and the transmission force. This parameter represented the wave propagation time (speed of sound) in the material. The specific convergence of the dynamic forces was evaluated at the earliest time, when the transmission force was equal to the incident force. For all the materials, the wave propagation time remained similar at all the impact velocities, whereas the specific convergence of dynamic forces occurred earlier at the medium and the high impact velocity. Thus, the equilibrium of dynamic forces was achieved in a shorter time than in the case of the low impact velocity. As the wave propagation time remained approximately constant for all the impact velocities and was much lower than the specific convergence, the stress wave in the specimen had to be more dispersed through the volume

Dynamic penetration of cellular solids: Experimental investigation
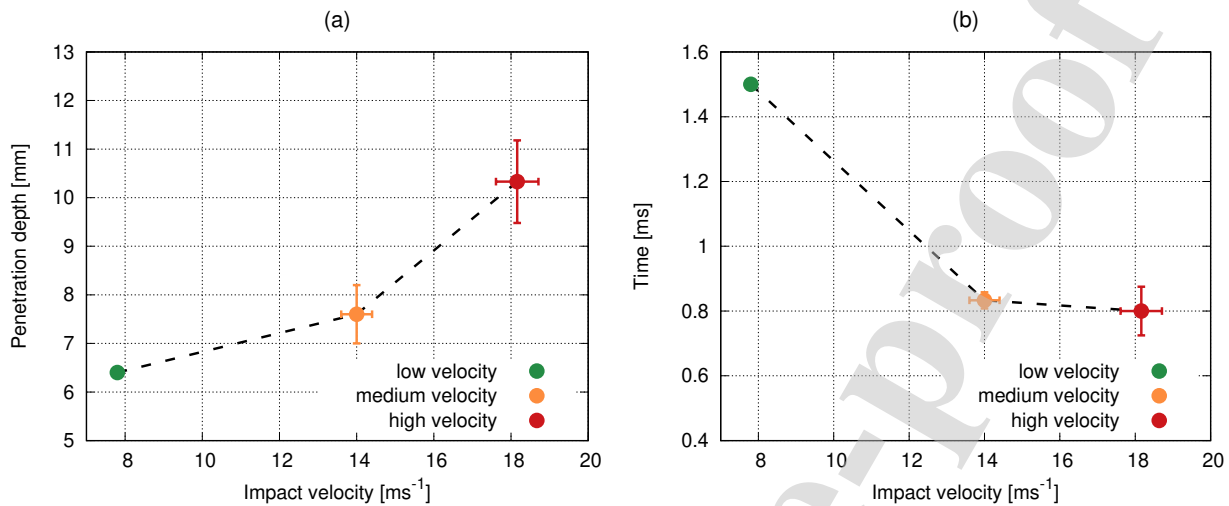
Figure 10: (a) Penetration depth, where the disintegration of the APM foam occurred, plotted against the initial impact velocity. (b) Time, when the disintegration of the APM foam occurred, plotted against the initial impact velocity.
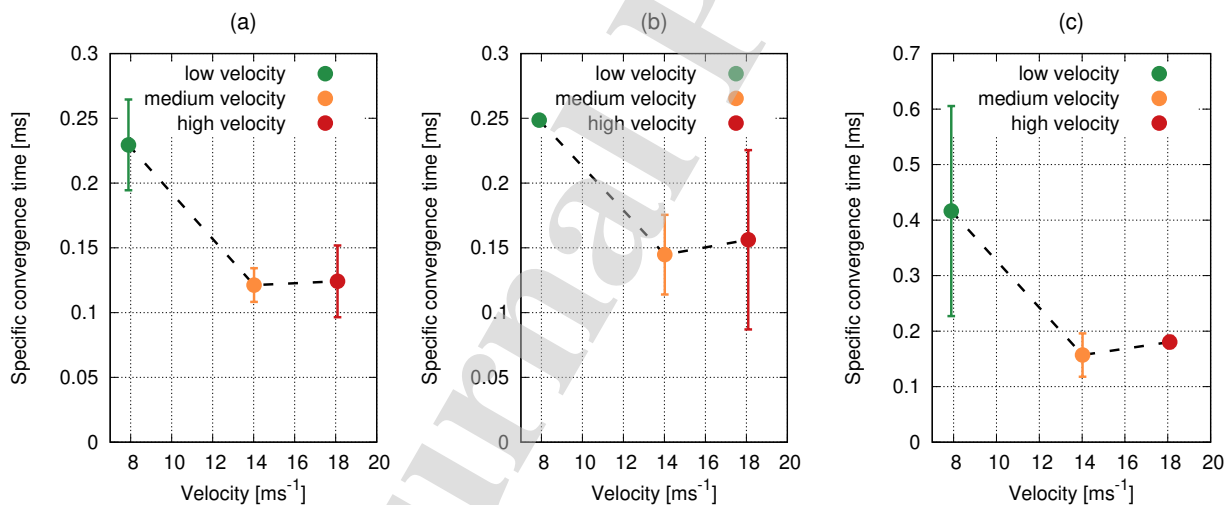
Figure 11: Specific convergence time of the dynamic forces: (a) the closed-cell aluminium foam, (b) the hAPM foam, (c) the APM foam.

of the specimen at the low impact velocity and more localized at the two higher velocities. Specific convergence of the dynamic forces for the closed-cell aluminium foam is shown in Fig. 11a, for the hAPM foam in Fig. 11b, and for the APM foam in Fig. 11c.

3.5. XCT results
3.5.1. Closed-cell foam

The differential XCT analysis of the closed-cell foam sample was performed on the basis of both the subtraction of the volumes and using the blending of volumes due to the different character of the closed-cell foam internal structure. Here, the subtraction of the loaded volume from the 3D image of intact state can be used to isolate the porous microstructure under the final position of the impactor, as the unloaded volume subtracted from the 3D image of the

Dynamic penetration of cellular solids: Experimental investigation
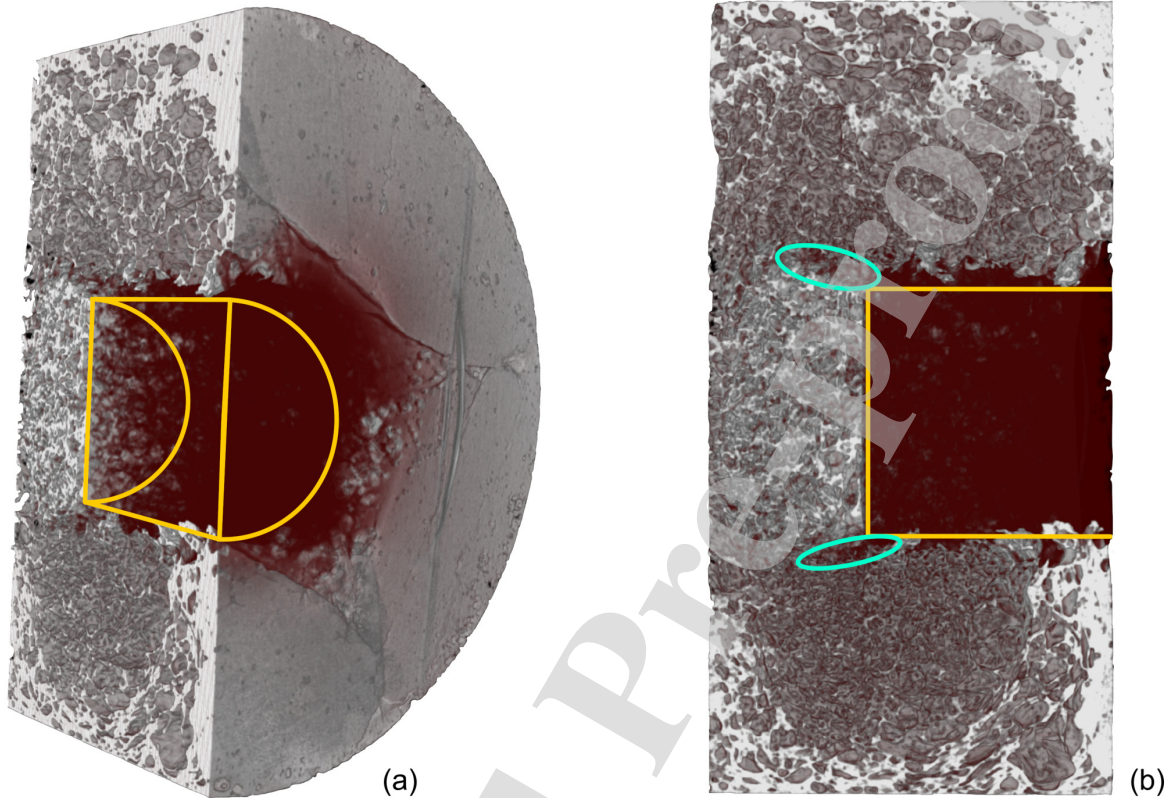
Figure 12: Perspective 3D visualisation of penetrated closed-cell foam sample showing overlapping penetrated sample (white) and the influenced volume (dark red) - view along the penetrating bar (a) and visualisation in the medial plane (b).

impacted state allows evaluating differences along the path of the impactor. Still, particularly the damaged parts of microstructure in the vicinity of the penetrating bar and around the compacted region shown in the following paragraphs remained hidden. This was caused partially due to different intensity range of both volumes caused by the stacked imaging of multiple samples at a time leading to a considerably low signal-to-noise ratio in the 3D images after subtraction. The Fig. 12 depicts 3D visualisation of the impacted specimen, which is simply combined with the aligned volume of the intact specimen.

In Fig. 12, the penetrated volume is light-grey, the material of the intact foam prior to mechanical testing is dark-red and graphical elements are included for better orientation. The figure on the left shows half of the foam specimen obtained by performing sectioning in the medial plane with the viewpoint set to capture the path of the impactor and the figure on the right is the direct view on the medial-plane section. The amber graphics represents then the geometry of the penetrating bar and the cyan ellipses highlight the visible interesting features in the microstructure of the penetrated volume. Because of the microstructure constituted by thin cell-struts from a homogeneous metal alloy, the formation of a damaged envelope caused by the deformation energy concentrated directly under the impacting bar can hardly be identified. Hence, 2D visualisations of slices through the reconstructed volume in the medial and transversal plane was studied, see Fig. 13(a-c) and Fig. 13(d,e).

The Fig. 13(a-c) shows slices in the medial plane in the intact and loaded specimen together with the slice in the blended volume. The amber graphics depicts the projection of impacting cylinder in the medial plane, i.e. the vertical lines correspond to the edge on the circular face of the impactor, while the horizontal lines depict the diameter of the bar. No deflection of the opposite, non-impacted, circular face of the specimen was observed in the image of the impacted specimen indicating that concurrence of the closed-cell metal foam microstructure and the integral metal skin resulted in strain-wave propagation into the transmission bar without plastic damage to the surrounding

Dynamic penetration of cellular solids: Experimental investigation
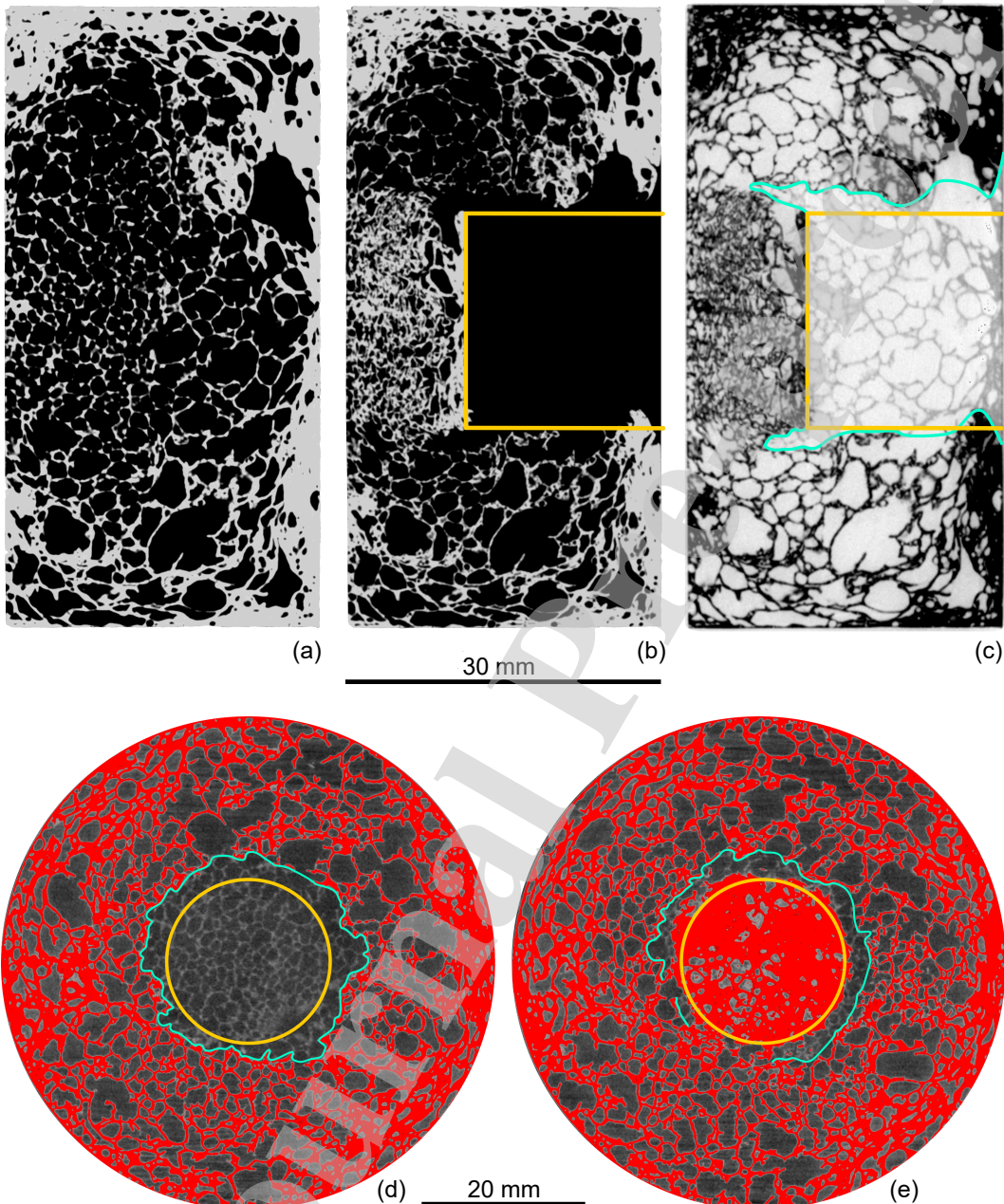
Figure 13: 2D visualisation of closed-cell foam sample: medial plane of the intact specimen (a), impacted specimen (b), and blended volume (c); blended volume in transversal plane in the penetrated region (d) and under the final position of impactor (e).

parts of the microstructure. The image of the impacted specimen also shows how the penetrating bar damaged the porous microstructure around the circumference of the bar that led to the failure of the cell-struts and opening of pores in the vicinity of the bar. However, more details are revealed by analysing the blended volume, where the white colour represents air contained in the pores. The microstructure of the impacted specimen is shown in black, and the microstructure within the intact specimen is depicted in grey. The cyan line highlights the void regions formed as a result of the bar penetration into the specimen showing the extent of open volume significantly exceeding the bar dimensions. It can be seen that the dimensions of the damaged region gradually increase with the penetration depth and

Dynamic penetration of cellular solids: Experimental investigation
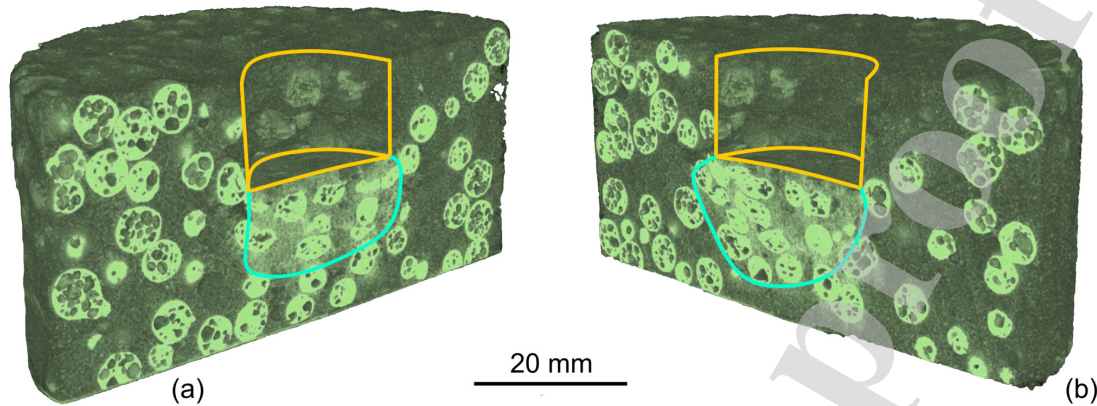
Figure 14: Perspective 3D visualisation of penetrated hAPM foam sample showing medial (a) and frontal (b) plane sections through the volume of the sample.

continue up to 4 mm below the final penetration depth achieved in the experiment. The shape of the resulting cavity shows significant localized shear-stress induced damage leading to approximately 11° deviation of the failed cell-struts region from the axis of penetration. The region of densified foam structure composed in majority of collapsed cells then forms deformed envelope of the microstructure having the cylindrical geometry in this case. Its boundaries can be clearly seen in the blended volume as the region with the smallest cell-volume under the impactor. The cyan graphics around the bar projection near the impacted face of the specimen shows plastic deformation of integral metal skin developed during bar penetration resulting in 28.4 mm outer diameter of the opening. However, the conclusions made only from the analysis of the visualisation in the medial plane may be misleading due to the stochastic nature of the material microstructure. Thus, the blended volume was additionally investigated in the transversal plane as shown in Fig. 13(d,e). The left slice is located 1.3 mm above and the right slice is located 0.3 mm under the final position of the bar. The amber graphics depicts the circumference of the impacting bar and the cyan curves highlight the void space around the impactor in the left slice and around the deformed envelope in the right slice. It can be seen that both the geometry of the void space created by the impacting bar is relatively uniform with the diameter of the circle approximating the void space boundaries of 24 mm. Except for the 90° sector in the top-left direction, the dimensions of the impacting bar in the region of the accumulated material near the final penetration depth are not exceeded by homogeneous material and only local protrusions can be observed.
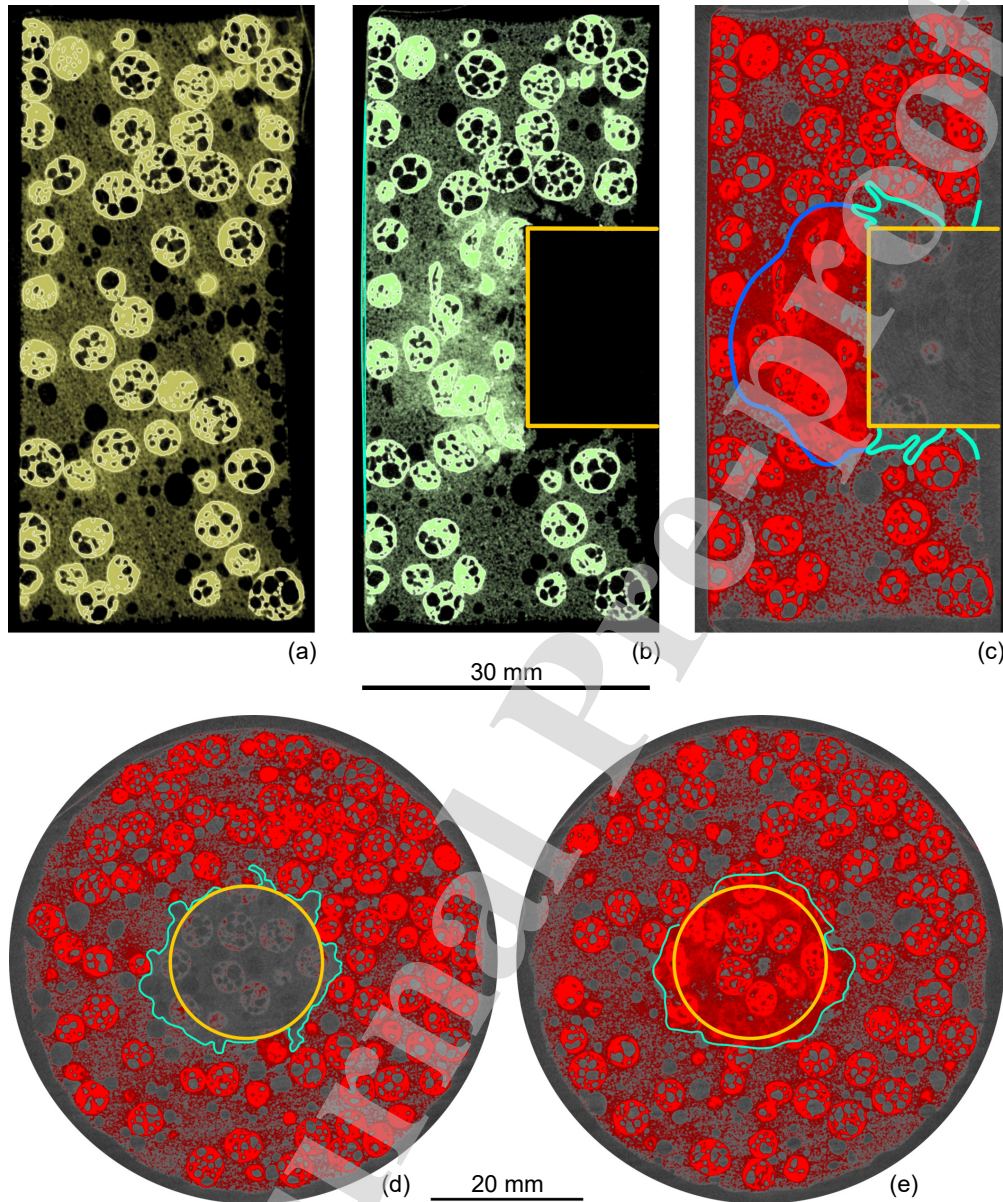
3.5.2. hAPM foam

The differential XCT analysis of the hAPM foam sample and visualisation of the results was performed from the blended volume, because the subtraction of the reference and deformed volume resulted in very low signal-to-noise ratio in the 3D image due to the presence of epoxy matrix in the microstructure. Unlike the closed-cell metal foam sample, where the complex microstructure composed of a high number of cells makes the interpretation difficult, the effects induced by the medium-rate dynamic impact into the hAPM foam can be studied also from the sections in the 3D reconstructed image of the loaded state as depicted in Fig. 14.

In the Fig. 14, the approximate dimensions of the impacting bar in its final position after penetration are provided graphically using the amber contours. Since the visualisation is derived from the full intensity range, it is interesting to study also the possible changes in the epoxy matrix. By comparing the appearance of the region directly under the impactor and in the volume around its outer edges, it can be seen that the region under the impactor exhibits a higher density of the material, where the extent of the region of the compacted matrix is depicted by the cyan colour. The highlighted geometry of the compacted region can be assumed approximately spheroid in the whole volume with the circle representing the intersection of the cylindrical impactor with the compacted region forming a spherical dome geometry. However, due to the homogeneity of the epoxy matrix, the microstructural changes in the vicinity of the impactor can not be studied using the 3D visualisation of the reconstructed 3D images. For this reason, 2D visualisations of slices through the reconstructed volume in medial and transversal plane were studied, see Fig. 15(a-c)

Dynamic penetration of cellular solids: Experimental investigation

Figure 15: 2D visualisation of hAPM foam sample: medial plane of the intact specimen (a), impacted specimen (b), and blended volume (c); blended volume in transversal plane in the penetrated region (d) and under the final position of impactor (e).

and Fig. 15(d,e).

The Fig. 15(a-c) shows slices in the medial plane in the intact and loaded specimen together with the slice in the blended volume. The amber graphics depicts the projection of impacting cylinder in the medial plane. In the visualisation of the intact specimen, the apparent 2.5 mm deflection of the right impacted the face of the sample influencing the evaluation of mechanical results is apparent aside from the aluminium sphere distribution and the voids in the epoxy matrix. In the image of the impacted specimen, the cyan graphical elements depict the identified 0.75 mm deflection of the opposite, non-impacted, circular face of the specimen. The same material density (image intensity) variations in the epoxy matrix under the final position of the impactor observed in the 3D visualisation are also apparent, although the projected geometry is closer to a wedge rather than elliptical or circular section. Further details are revealed though,

when the blended volume is analysed. The blue line depicts precisely the compacted region under the impactor, which exhibits the circular shape except for the lobes near the positions corresponding to the radius of the bar. However, the shape of the compacted region is in this case apparently influenced by the displaced and deformed aluminium spheres causing the more complex material response to impact. The cyan graphics highlights in this figure the void regions formed as a result of the bar penetration into the specimen. The total diameter of open volume after loading not only significantly exceeds the bar dimensions, but the shape of the cavity also shows significant localized shear-stress induced damage of the epoxy matrix geometrically similar to shock-wave propagation characteristics. The damage evolution is concentrated along with two apparent directions and the cavity formation, in either case, is stopped by the presence of aluminium spheres. The two vertices of the void closer to the impacting bar reaching the depth under the final position of the impactor then undergo a smooth transition into the deformed envelope of the matrix circumventing the displaced aluminium spheres similarly to the deformed envelope region itself. Furthermore, the cyan graphics around the bar projection near the impacted face of the specimen shows plastic deformation of matrix developed during bar penetration resulting in the plasticized area with a diameter of 25.9 mm. However, the conclusions made only from the analysis of the visualisation in the medial plane may be misleading due to the stochastic nature of the material microstructure. Thus, blended volume was investigated in the transversal plane as shown in Fig. 15(d,e). The left slice is located 1.8 mm above and the right slice is located 2.0 mm under the final position of the bar. The amber graphics depicts the circumference of the impacting bar and the cyan curves highlight the void space around the impactor in the left slice together with the extent of the deformed envelope in the right slice. It can be seen that the geometry of both void space created by the impacting bar and the deformed envelope under its face strongly depends on the angular position of the section used to visualise the internal structure in perpendicular direction.

4. Discussion and Conclusion

The results of the OHPB based dynamic penetration tests lead to the following findings and remarks:

- Straight-forward wave separation technique was employed to evaluate the forward and backward propagating waves in the setup and allowed for the investigation of the deformation behaviour in a longer time window. In all conducted experiments, the wave separation technique provided valid and precise results for a number of wave reflections. The separation was always successful at least until the end of the experiment, i.e., to the point, when the impact velocity decreased to zero. Using the utilized instrumentation, wave propagation analysis during the penetration process was possible even at impact velocities close to 20 ms^{-1}. If the distance between the impact face and strain-gauge is sufficient to form a homogeneous strain-wave, the method can be used for instrumented testing with different types of impactors. For the incident bar used in the experiments, the inverse of the introduced wave separation method could be used to process the DIC data and roughly estimate the actual force by reconstruction of the wave propagation behaviour in the bar. However, this was not possible for shorter striker bars as the individual waves in the bar could not be identified.

- Wave propagation through the specimens played a crucial role in the deformation mode of the tested cellular materials and had a significant influence on the corresponding force-displacement diagrams as well as on the energy absorption characteristics. Based on the acquired results, the wave propagation and dispersion effects are considered more important at low impact velocities. All the tested materials exhibited the longest time to specific force convergence (equal incident and transmission force) at the lowest impact velocity where the effects of wave dispersion are more pronounced, while the strain wave propagates approximately homogeneously throughout the volume of the sample without localization under the impactor. Some specimens of the APM foam and the hAPM foam did not reach specific force convergence during the whole impact. The time of the specific convergence decreased for all the materials at higher impact velocities and the highest values of the specific time convergence were observed for the APM foam. The APM foam exhibited the lowest mechanical impedance related to its structure with hollow spheres embedded in the weak matrix. The significant increase in the wave convergence time was observed between the intermediate and high impact speed scenario, which can be attributed to the dynamic nature of the loading, where time-to-convergence is typically proportional to impact speed.

- All the materials exhibited a certain level of decrease in penetration force in the initial penetration phase with increasing impact velocity, which is a disadvantageous property in terms of impact protection capabilities. This effect was the most pronounced in case of the closed-cell foam and it had a crucial influence on its deformation

Dynamic penetration of cellular solids: Experimental investigation

behaviour particularly at low impact velocities. On the other hand, the effect was marginal for the APM foam and the hAPM foam as the standard deviations of the piercing force partially overlap. In general, the closed-cell metal foam exhibited deformation behaviour common to the standard metal foams showing significant plateau region (after the initial phase of the penetration), whereas the other two composite materials exhibited approximately linear dependency of penetration force with penetration depth. Although the hAPM foam did not exhibit plateau region, its energy absorption capability was comparable with the closed-cell foam despite its lower mass density, while the penetration force was only slightly higher.

- The effect of wave propagation was the most significant for the closed-cell aluminium foam, where the penetration force in the initial phase was the highest for the lowest impact velocity. This finding, not observed in the dynamic compression of the material [12, 16] and even in dynamic penetration of the similar materials without an integral skin over the foam core [46, 55], was found to be connected with the damage mechanisms on the surface of the specimen and wave propagation through its volume. During the penetration at low velocity, the integral skin over the core of the specimen was penetrated smoothly (or the skin was not perforated at all), the deformation was not localized to the close vicinity of the projectile but rather spread out through the front face of the specimen and the stress wave was more dispersed through the volume of the specimen. With the increasing impact velocity, this effect was suppressed and the force-displacement relationship was closer to the standard behaviour of the closed-cell aluminium foam. The surface skin was penetrated abruptly and the wave propagation was very localized. Similar behaviour was described for penetration of the compact as well as the sandwich panels [93]. In such a case, the transition velocity defining the change in the deformation behaviour from transient to more localized can be identified. The transition velocities for standard materials are much higher than those observed in our case. However, the values identified in the experiments were in good agreement with the energy-related change of behaviour described in literature [57] and with studies analyzing shock and wave propagation localized behaviour [13, 29]. The findings are not contrary to the studies characterizing the closed-cell foams during dynamic penetration [46, 55] as well as in dynamic compression [29, 13, 55]. After the initial penetration phase, similar effects were observed.

Therefore, in our opinion, the behaviour observed in the first part of the penetration is related to the presence of the skin over the foam. We have used the data from the overview high-speed camera to investigate surface area affected during the impact. The representative case of the specimen penetrated at the low impact velocity is compared with the specimen penetrated at the high impact velocity in Fig. 16. The affected area was determined as the area with visibly changing the front face of the specimen during the impact. An in-house script was developed to identify the changes on the front face of the specimen. As can be seen in Fig. 17a, the identified affected area is significantly larger for the lower impact velocity than for the other two velocities. The increased affected area at the low-velocity impact supports the conclusion that the higher strength of the closed-cell aluminium foam at the low impact velocity is related to the wave propagation and dispersion through the specimen volume while, at the higher velocities, the wave propagation is more localized under the penetrating projectile. During most of the impacts at low velocity, the front face was not penetrated, but rather bent inwards.

Furthermore, the DIC was used to identify the longitudinal strain on the specimen's surface. A grid of correlation points was established on the surface of the specimen and the incremental longitudinal strain was evaluated using the calculated displacements. As it can be seen in Fig. 17b, the longitudinal strain is nonzero in case of the penetration at the low velocity whereas no longitudinal strain was identified in the specimen penetrated at the high impact velocity. This finding supports the conclusion that with the increasing velocity, the penetration is more localized and concentrated under the impacting object whereas at the low impact velocity the whole specimen is deformed to some extent.

- In terms of the ability of the investigated materials to perform as a protection against an object penetrating their microstructure, the closed-cell aluminium foam remained compact and was able to effectively absorb the impact energy at all tested impact velocities. The APM foam was found not suitable for penetration protection as the material exhibited a strong tendency to disintegration at medium and high velocities. The weak matrix can not withstand the loads and the material was predominantly damaged by the separation at the boundaries. Inertia effects also played a crucial role during the penetration of the specimens. Penetration depth at the disintegration of the APM foam increased with the impact velocity. However, time to disintegration was approximately constant for both the medium and the high impact velocity. Therefore, the higher penetration depth at disintegration was

Dynamic penetration of cellular solids: Experimental investigation
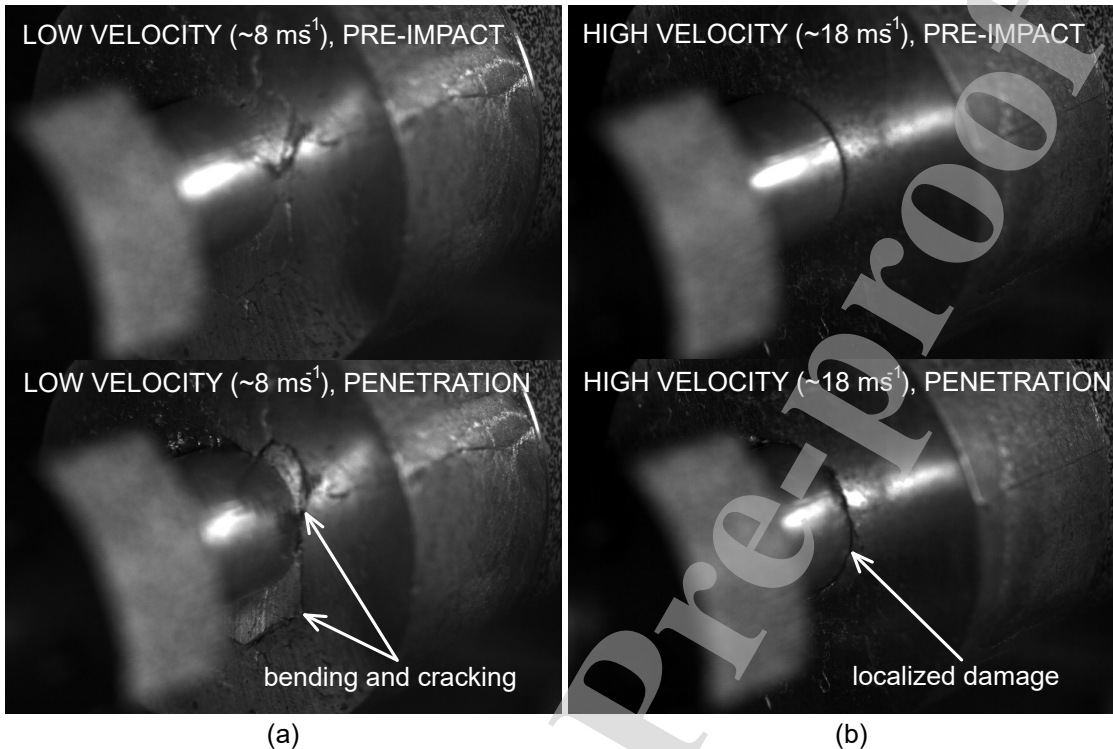
Figure 16: The representative case of the closed-cell aluminium foam specimen penetrated at: (a) the low impact velocity compared with (b) the specimen penetrated at the high impact velocity. Note the affected area during the impact at low velocity.

related to the inertia effects as a given period of time was necessary to disintegrate the specimen. The increase in load capacity of the APM foam with the impact velocity was related only to the dynamic nature of the testing as inertia prevented their immediate disintegration, when the maximum load capacity was exceeded.

- The closed-cell foam sample and the hAPM sample was successfully subjected to the differential CT procedure for detailed analysis of microstructural variations resulting from the bar dynamically penetrating through the internal structure of the materials. It was possible to quantify the shape and dimensions of the cavity created by the impacting bar and the related effects resulting from strain-wave propagation through the specimen and also the characteristics of the deformed envelopes formed under the final position of the penetrator. However, it is evident that complex XCT imaging campaign should be performed to include preferably the intact-impacted specimen pairs from all the performed penetration experiments, i.e., the quasi-static and all the dynamic impacts, to obtain thorough information on deformation processes present during the loading procedures. Here, our initial assumption that the differential CT of the specimens subjected to the intermediate impact speed would be capable to reveal the relevant deformation mechanisms in the penetrated materials was not confirmed and particularly the tomographical analysis of low-velocity penetration would bring important advantage in the interpretation of mechanical and DIC results.

- In the closed-cell foam sample, the uniform homogeneous pore-size distribution was observed only in the core region of the samples, while the integral metal skin not only caused a significant increase of the complexity of the deformation process by introducing different mechanisms of load transfer in dependence of impact speed, but also porosity in the majority of the sample volume was affected. The blending procedure of the intact and impacted volume provided hard evidence on the difference between the truly displaced or damaged cell-struts and the pores that were only opened by the penetrating bar. It can be also noticed that the two vertices of the void at the maximum depth of the opened cavity smoothly circumvent the densified envelope providing the

Dynamic penetration of cellular solids: Experimental investigation
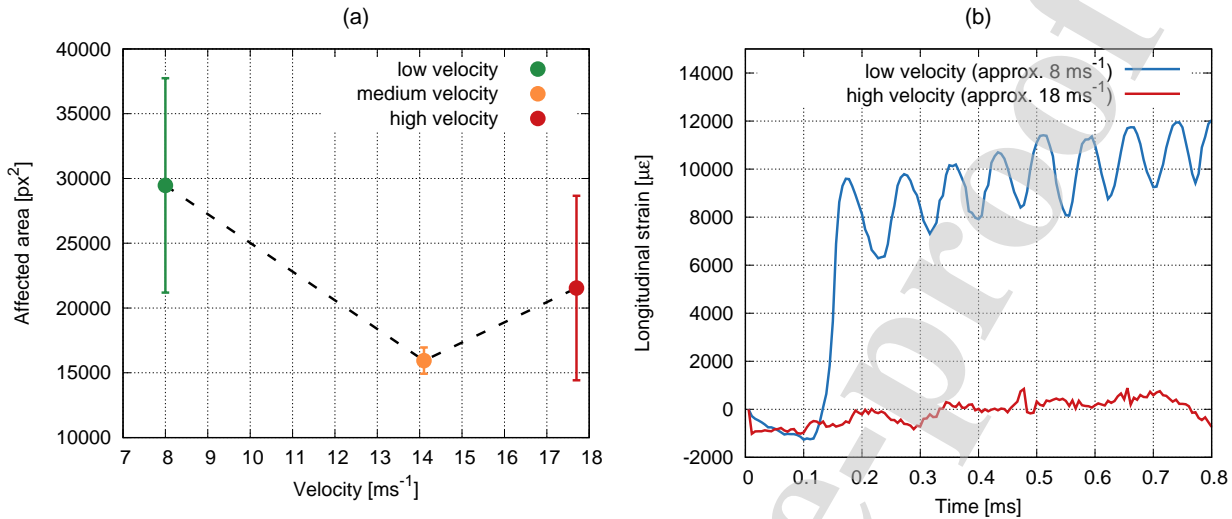
Figure 17: (a) Size of the area at the front face of the specimen affected by the impact. (b) Longitudinal strain evaluated using the DIC on the surface of the closed-cell aluminium foam specimen at two different impact velocities.

information about the strain wave path during the loading. The inspection of either the impacted or the blended volume shows that material is accumulated along the circular face of the impactor and around its edges, which is a combination of the metal skin itself separated from the face during contact of the bar with the specimen and the cell-wall material gathered during penetration of the bar. It can be reasonably assumed that this material accumulation is a mechanism supporting the shear failure of individual cell-struts as the effective diameter of the impactor (i.e., the diameter of the bar is enlarged gradually by the gathered material) increases along its path.

- The deformation response of the hAPM foam sample was influenced by non-uniform distribution of aluminium sphere particle reinforcement in the epoxy matrix, where higher sphere density was observed near the outer edges of the specimen, outside of the penetrated region. However, the differential CT showed that the presence of the aluminium spheres in the matrix acted as a barrier shaping the propagation of the strain-wave through the specimen and that it was a factor, which can be successfully utilized to control the deformation response of such material. In the tomographical images of the impacted volume, the observed intensity variation in the matrix under in the impactor is also independent on the displaced aluminium spheres originally distributed in the penetrated volume as only negligible low-energy photon scatter was present in the acquired projections. Thus, it can be assumed that such a region represents the result of kinetic energy dissipation into the impacted material resulting in compaction of the matrix. Furthermore, it can be inferred from these results that the aluminium spheres effectively shape and resist the wave propagation in the material, while mitigating the energy by their plastic deformation in the region under the impacting bar. The boundaries of the deformed envelope under the impactor are largely hidden by the presence of plastically deformed aluminium spheres and only rough estimation is possible from the 2D visualisations. In contrast, a 2D transverse visualisation is a useful tool for evaluation of the void space geometry as shown by its boundaries depicted by the cyan curve in the left part of the figure. In this orientation of visualisation, the apparently larger amount of the aluminium spheres is concentrated right from the vertical axis of symmetry. The presence of the aluminium spheres and their influence on the formation of the void region can be successfully studied. When comparing cyan highlighted regions left and right from the vertical axis of symmetry, only one continuous void was created in the region containing only the epoxy matrix without the sphere reinforcement. On the other side, three isolated regions were created and in every case, the extent of the void space was limited by the presence of the reinforcement. This supports the previous finding that the aluminium sphere reinforcement in the hAPM foam and its distribution can be used to control the transmission of the strain wave through the microstructure and influences the foam's deformation energy absorption capacity.

Dynamic penetration of cellular solids: Experimental investigation

- Using the combination of mechanical testing, optical inspection of specimens, DIC evaluation of optical data, and the XCT analysis, it has been demonstrated that the investigated materials are more susceptible to penetration with the increase of the impact speed, which is related to the shorter wave propagation times due to the deformation and damage localized in the vicinity of the impacting object. The impactor then penetrates the microstructure to a higher depth, while the surrounding material remains intact and has no influence on the mechanical response of the samples. Owing to the epoxy matrix and the distribution of aluminium spheres, only the hAPM foam showed an increase in dissipated deformation energy with the high impact velocity despite the inversely proportional dependency of the absorbed energy at the depth of 3.5 mm on the impact velocity. The APM foam, composed of aluminium spheres with point-like connectivity given by the polyamide matrix, was observed to be prone to disintegration resulting from shear stress and inertia effects induced damage to the matrix disqualifying the material in the current state from its use in the deformation energy mitigation measures. However, the confinement of the APM foam in appropriate encasement would change the deformation characteristics considerably. In the same sense, the closed-cell foam exhibited measurable dependence of the results on the impact velocity as a result of the influence of the metal skin. Similarly, the modification of the metal skin properties making it functional in the stress distribution also in the higher impact velocities would significantly improve the overall performance of the closed-cell foam in the considered loading scenarios.Nevertheless, based on the high-resolution XCT and the differential CT procedures, it has been shown that the results can be used, in case of both the closed-cell foam and hAPM foam, for improvement of the production processes as the radiographical inspection of the internal structure pointed out problems arising from limited control of the production process. In case of the APM foam modified with the outer confining layer, the XCT evaluation would also be an essential tool for inspection of its microstructure both before and after the impact loading.

Conclusion

The modified OHPB with full two-sided instrumentation was used to penetrate the specimens at three different impact velocities ranging from $8\,\mathrm{ms^{-1}}$ to $18\,\mathrm{ms^{-1}}$. The wave separation technique was employed to process the strain-gauge signals and to extend the usable time window of the Hopkinson bar experiment to cover the entire duration of the impact. Wave propagation phenomena, inertia effects, energy absorption and localization of the damage were in detail investigated for all types of the tested materials. It was found out that the time required for convergence of the dynamic forces at both faces of the specimen was the highest for the lowest impact velocity. This effect was related to the wave propagation in the specimen as, at low impact velocities, the stress-wave was more dispersed through the volume of the specimens. With increasing impact velocity, the damage was more localized underneath the projectile. This effect was the most profound for the closed-cell aluminium foam with integral skin covering the foam core. During the initial phase of the penetration at low velocities, the wave propagation related effects were considered more important than other effects such as possible strain-rate sensitivity of the material. Inertia effects also play an important role as, e.g., the APM foam disintegrated with increasing impact velocity at higher penetration depths. However, it was identified that this behaviour was related to the inertia effects preventing immediate disintegration of the specimen, when its loading capacity was exceeded. Differential XCT was successfully employed for a pre- and post-impact volumetric analysis of the specimens and supported the conclusions evaluated using the strain-gauge and DIC data. Altogether, the discussed effects can significantly affect the strength and deformation behaviour of the cellular materials during dynamic indentation, where the complex loading of the structure is different than during the dynamic uni-axial loading.

Dynamic penetration of cellular solids: Experimental investigation

Data Availability

The raw/processed data required to reproduce these findings cannot be shared at this time due to technical or time limitations.

References

[1] Lorna J Gibson and Michael F Ashby. *Cellular solids: structure and properties*. Cambridge university press, 1999.

[2] J. Zhang, Q. Qin, S. Chen, Y. Yang, Y. Ye, C. Xiang, and T.J. Wang. Low-velocity impact of multilayer sandwich beams with metal foam cores: Analytical, experimental, and numerical investigations. *Journal of Sandwich Structures and Materials*, 22(3):626–657, 2020.

[3] X. Tan, B. Wang, Y. Yao, K. Yao, Y. Kang, S. Zhu, S. Chen, and P. Xu. Programmable buckling-based negative stiffness metamaterial. *Materials Letters*, 262, 2020.

[4] P. Jiao, S. M. Nicaise, M. Azadi, J. Cortes, D. E. Lilley, W. Cha, P. K. Purohit, and I. Bargatin. Tunable tensile response of honeycomb plates with nanoscale thickness: Testing and modeling. *Extreme Mechanics Letters*, 34, 2020.

[5] Y. Jiang, Z. Liu, N. Matsuhisa, D. Qi, W. R. Leow, H. Yang, J. Yu, G. Chen, Y. Liu, C. Wan, Z. Liu, and X. Chen. Auxetic mechanical metamaterials to enhance sensitivity of stretchable strain sensors. *Advanced Materials*, 30(12), 2018.

[6] J. Lankford Jr. and K. A. Dannemann. Strain rate effects in porous materials. In *Materials Research Society Symposium - Proceedings*, volume 521, pages 103–108, 1998.

[7] R. Smerd, S. Winkler, C. Salisbury, M. Worswick, D. Lloyd, and M. Finn. High strain rate tensile testing of automotive aluminum alloy sheet. *International Journal of Impact Engineering*, 32(1-4):541–560, 2005.

[8] M. Vesenjak, C. Veyhl, and T. Fiedler. Analysis of anisotropy and strain rate sensitivity of open-cell metal foam. *Materials Science and Engineering: A*, 541:105 – 109, 2012.

[9] G. Imbalzano, P. Tran, T. D. Ngo, and P. V. S. Lee. Three-dimensional modelling of auxetic sandwich panels for localised impact resistance. *Journal of Sandwich Structures and Materials*, 19(3), 2017.

[10] Yoshihiko Hangai, Naoyuki Kubota, Takao Utsunomiya, Hisanobu Kawashima, Osamu Kuwazuru, and Nobuhiro Yoshikawa. Drop weight impact behavior of functionally graded aluminum foam consisting of a1050 and a6061 aluminum alloys. *Materials Science and Engineering: A*, 639:597 – 603, 2015.

[11] V.S. Deshpande and N.A. Fleck. High strain rate compressive behaviour of aluminium alloy foams. *International Journal of Impact Engineering*, 24(3):277 – 298, 2000.

[12] M. Peroni, G. Solomos, and V. Pizzinato. Impact behaviour testing of aluminium foam. *International Journal of Impact Engineering*, 53:74 – 83, 2013. Special issue based on contributions at the 3rd International Conference on Impact Loading of Lightweight Structures.

[13] Pengfei Wang, Songlin Xu, Zhibin Li, Jinglei Yang, Chao Zhang, Hang Zheng, and Shisheng Hu. Experimental investigation on the strain-rate effect and inertia effect of closed-cell aluminum foam subjected to dynamic loading. *Materials Science and Engineering: A*, 620:253 – 261, 2015.

[14] Marco Peroni, George Solomos, and Norbert Babcsan. Development of a hopkinson bar apparatus for testing soft materials: application to a closed-cell aluminum foam. *Materials*, 9(1):27, 2016.

[15] R.P. Merrett, G.S. Langdon, and M.D. Theobald. The blast and impact loading of aluminium foam. *Materials & Design*, 44:311 – 319, 2013.

[16] Xin Pang and Hejun Du. Dynamic characteristics of aluminium foams under impact crushing. *Composites Part B: Engineering*, 112:265 – 277, 2017.

[17] Sergey L. Lopatnikov, Bazle A. Gama, Md. [Jahirul Haque], Carl Krauthauser, John W. Gillespie, Mustafa Guden, and Ian W. Hall. Dynamics of metal foam deformation during taylor cylinder–hopkinson bar impact experiment. *Composite Structures*, 61(1):61 – 71, 2003.

[18] Masatoshi Nishi, Shigeru Tanaka, Matej Vesenjak, Zoran Ren, and Kazuyuki Hokamoto. Experimental and computational analysis of the uni-directional porous (unipore) copper mechanical response at high-velocity impact. *International Journal of Impact Engineering*, 136:103409, 2020.

[19] R. Rajendran, A. Moorthi, and S. Basu. Numerical simulation of drop weight impact behaviour of closed cell aluminium foam. *Materials & Design*, 30(8):2823 – 2830, 2009.

[20] M. Altenaiji, Z.W. Guan, W.J. Cantwell, Y. Zhao, and G.K. Schleyer. Characterisation of aluminium matrix syntactic foams under drop weight impact. *Materials & Design*, 59:296 – 302, 2014.

[21] A Paul and U Ramamurty. Strain rate sensitivity of a closed-cell aluminum foam. *Materials Science and Engineering: A*, 281(1):1 – 7, 2000.

[22] G.W. Ma, Z.Q. Ye, and Z.S. Shao. Modeling loading rate effect on crushing stress of metallic cellular materials. *International Journal of Impact Engineering*, 36(6):775 – 782, 2009.

[23] A. Jung, A. D. Pullen, and W. G. Proud. Strain-rate effects in Ni/Al composite metal foams from quasi-static to low-velocity impact behaviour. *Composites Part A: Applied Science and Manufacturing*, 85:1–11, 2016.

[24] Bing Hou, H Zhao, S Pattofatto, JG Liu, and YL Li. Inertia effects on the progressive crushing of aluminium honeycombs under impact loading. *International Journal of Solids and Structures*, 49(19-20):2754–2762, 2012.

[25] Jae Ung Cho, Soon Jik Hong, Sang Kyo Lee, and Chongdu Cho. Impact fracture behavior at the material of aluminum foam. *Materials Science and Engineering: A*, 539:250 – 258, 2012.

[26] Dejan Tomazincic, Branko Necemer, Matej Vesenjak, and Jernej Klemenc. Low-cycle fatigue life of thin-plate auxetic cellular structures made from aluminium alloy 7075-t651. *Fatigue & Fracture of Engineering Materials & Structures*, 42(5):1022–1036, 2019.

[27] Mehdi Taherishargh, Bálint Katona, Thomas Fiedler, and Imre Norbert Orbulov. Fatigue properties of expanded perlite/aluminum syntactic foams. *Journal of Composite Materials*, 51(6):773–781, 2017.

[28] C.Q. Xi and Q.M. Li. Meso-scale mechanism of compaction shock propagation in cellular materials. *International Journal of Impact Engineering*, 109:321 – 334, 2017.

Dynamic penetration of cellular solids: Experimental investigation

[29] I. Elnasri, S. Pattofatto, H. Zhao, H. Tsitsiris, F. Hild, and Y. Girard. Shock enhancement of cellular structures under impact loading: Part I experiments. *Journal of the Mechanics and Physics of Solids*, 55(12):2652 – 2671, 2007.

[30] Sergey L. Lopatnikov, Bazle A. Gama, Md.Jahirul Haque, Carl Krauthauser, and John W. Gillespie. High-velocity plate impact of metal foams. *International Journal of Impact Engineering*, 30(4):421 – 445, 2004.

[31] Zhijun Zheng, Yaodong Liu, Jilin Yu, and Stephen R. Reid. Dynamic crushing of cellular materials: Continuum-based wave models for the transitional and shock modes. *International Journal of Impact Engineering*, 42:66 – 79, 2012.

[32] V.P.W. Shim, K.Y. Yap, and W.J. Stronge. Effects of nonhomogeneity, cell damage and strain-rate on impact crushing of a strain-softening cellular chain. *International Journal of Impact Engineering*, 12(4):585 – 602, 1992.

[33] Thomas Tancogne-Dejean, Adriaan B Spierings, and Dirk Mohr. Additively-manufactured metallic micro-lattice materials for high specific energy absorption under static and dynamic loading. *Acta Materialia*, 116:14–28, 2016.

[34] C. P. de Jonge, H. M. A. Kolken, and A. A. Zadpoor. Non-auxetic mechanical metamaterials. *Materials*, 12(4), 2019.

[35] Nejc Novak, Matej Vesenjak, Shigeru Tanaka, Kazuyuki Hokamoto, and Zoran Ren. Compressive behaviour of chiral auxetic cellular structures at different strain rates. *International Journal of Impact Engineering*, 141:103566, 2020.

[36] T. C. Lim, A. Alderson, and K. L. Alderson. Experimental studies on the impact properties of auxetic materials. *Physica Status Solidi B – Basic Solid State Physics*, 251(2):307–313, 2014.

[37] Olly Duncan, Leon Foster, Terry Senior, Andrew Alderson, and Tom Allen. Quasi-static characterisation and impact testing of auxetic foam for sports safety applications. *Smart Materials and Structures*, 25(5):054014, 2016.

[38] T. Fila, P. Zlamal, O. Jirousek, J. Falta, P. Koudelka, D. Kytyr, T. Doktor, and J. Valach. Impact testing of polymer-filled auxetics using split hopkinson pressure bar. *Advanced Engineering Materials*, 19(10), 2017.

[39] Nejc Novak, Lovre Krstulovic-Opara, Zoran Ren, and Matej Vesenjak. Mechanical properties of hybrid metamaterial with auxetic chiral cellular structure and silicon filler. *Composite Structures*, 234:111718, 2020.

[40] Nejc Novak, Matej Vesenjak, and Zoran Ren. Auxetic cellular materials – a review. *Strojniški vestnik - Journal of Mechanical Engineering*, 62(9):485–493, 2016.

[41] J. Glinz, D. Kytyr, T. Fila, J. Sleichrt, A. Schrempf, D. Furst, J. Kastner, and S. Senck. In-situ compression test of artificial bone foams in controlled environment using x-ray micro-computed tomography. pages 48–51, 2019.

[42] T. Doktor, T. Fila, P. Zlamal, D. Kytyr, and O. Jirousek. High strain-rate compressive testing of filling materials for inter-penetrating phase composites. pages 21–24, 2019.

[43] Isabel Duarte, Matej Vesenjak, Lovre Krstulović-Opara, and Zoran Ren. Crush performance of multifunctional hybrid foams based on an aluminium alloy open-cell foam skeleton. *Polymer Testing*, 67:246–256, May 2018.

[44] Susana C. Pinto, Paula A.A.P. Marques, Matej Vesenjak, Romeu Vicente, Luis Godinho, Lovre Krstulovic-Opara, and Isabel Duarte. Characterization and physical properties of aluminium foam–polydimethylsiloxane nanocomposite hybrid structures. *Composite Structures*, 230:111521, 2019.

[45] M. Neuhauserova, P. Koudelka, J. Falta, M. Adorna, T. Fila, and P. Zlamal. Strain-rate and printing direction dependency of compressive behaviour of 3D printed stainless steel 316l. pages 68–72, 2019.

[46] I. Elnasri and H. Zhao. Impact perforation of aluminium cymat foam. *International Journal of Mechanical Sciences*, 150:79 – 89, 2019.

[47] J. Zhou, Z.W. Guan, and W.J. Cantwell. The impact response of graded foam sandwich structures. *Composite Structures*, 97:370 – 377, 2013.

[48] A.U. Ude, A.K. Ariffin, and C.H. Azhari. Impact damage characteristics in reinforced woven natural silk/epoxy composite face-sheet and sandwich foam, coremat and honeycomb materials. *International Journal of Impact Engineering*, 58:31 – 38, 2013.

[49] Ali Kurşun, Mehmet Şenel, Halil M. Enginsoy, and Emin Bayraktar. Effect of impactor shapes on the low velocity impact damage of sandwich composite plate: Experimental study and modelling. *Composites Part B: Engineering*, 86:143 – 151, 2016.

[50] Qinghua Qin and T.J. Wang. Low-velocity impact response of fully clamped metal foam core sandwich beam incorporating local denting effect. *Composite Structures*, 96:346 – 356, 2013.

[51] M.A. Islam, M.A. Kader, P.J. Hazell, J.P. Escobedo, A.D. Brown, and M. Saadatfar. Effects of impactor shape on the deformation and energy absorption of closed cell aluminium foams under low velocity impact. *Materials & Design*, 191:108599, 2020.

[52] Shaoyu Hou, Tiantian Li, Zian Jia, and Lifeng Wang. Mechanical properties of sandwich composites with 3D-printed auxetic and non-auxetic lattice cores under low velocity impact. *Materials & Design*, 160:1305 – 1321, 2018.

[53] Nejc Novak, Luka Starčevič, Matej Vesenjak, and Zoran Ren. Blast response study of the sandwich composite panels with 3D chiral auxetic core. *Composite Structures*, 210:167 – 178, 2019.

[54] Sigit P. Santosa, Faizal Arifurrahman, Moh. Hafidz Izzudin, Djarot Widagdo, and Leonardo Gunawan. Response analysis of blast impact loading of metal-foam sandwich panels. *Procedia Engineering: Plasticity and Impact Mechanics*, 173:495 – 502, 2017.

[55] Xin Pang and Hejun Du. Investigation on dynamic penetration of closed-cell aluminium foam using in situ deceleration measurement. *Composites Part B: Engineering*, 100:78 – 90, 2016.

[56] Bahman Taherkhani, Javad Kadkhodapour, Ali Pourkamali Anaraki, Mahmoud Saeed, and Haoyun Tu. Drop impact of closed-cell aluminum foam. *Journal of Failure Analysis and Prevention*, 2020.

[57] S Ramachandra, P Sudheer Kumar b, and U Ramamurty. Impact energy absorption in an al foam at low velocities. *Scripta Materialia*, 49(8):741–745, 2003.

[58] P. Koudelka, O. Jirousek, T. Fila, and T. Doktor. Compressive properties of auxetic structures produced with direct 3D printing. *Materiali in Tehnologije*, 50(3):311–317, 2016.

[59] A. Elmahdy and P. Verleysen. Challenges related to testing of composite materials at high strain rates using the split hopkinson bar technique. In *EPJ Web of Conferences*, volume 183, 2018.

[60] J. T. Hammer, T. J. Liutkus, J. D. Seidt, and A. Gilat. Using digital image correlation (DIC) in dynamic punch tests. *Experimental Mechanics*, 55(1):201–210, 2015.

[61] A. Gilat, T. E. Schmidt, and A. L. Walker. Full field strain measurement in compression and tensile split hopkinson bar experiments. *Experi-

mental Mechanics, 49(2):291–302, 2009.

[62] D. Fang, Y. Li, and H. Zhao. On the behaviour characterization of metallic cellular materials under impact loading. *Acta Mechanica Sinica/Lixue Xuebao*, 26(6):837–846, 2010.

[63] T. Fila, P. Koudelka, P. Zlamal, J. Falta, M. Adorna, M. Neuhauserova, J. Luksch, and O. Jirousek. Strain dependency of poisson's ratio of sls printed auxetic lattices subjected to quasi-static and dynamic compressive loading. *Advanced Engineering Materials*, 21(8), 2019.

[64] A. Gilat and J. D. Seidt. Dynamic material characterization using digital image correlation. 566:3–9, 2014.

[65] T. Fila, P. Zlamal, J. Falta, T. Doktor, P. Koudelka, D. Kytyr, M. Adorna, J. Luksch, M. Neuhauserova, J. Valach, and O. Jirousek. Testing of auxetic materials using hopkinson bar and digital image correlation. In *EPJ Web of Conferences*, volume 183, 2018.

[66] M. Adorna, S. Bronder, J. Falta, P. Zlamal, and T. Fila. Evaluation of Hopkinson bar experiments using multiple digital image correlation software tools. pages 1–5, 2019.

[67] M. Adorna, P. Zlamal, T. Fila, J. Falta, M. Felten, M. Fries, and A. Jung. Testing of hybrid nickel-polyurethane foams at high strain-rates using hopkinson bar and digital image correlation. pages 72–76, 2018.

[68] R. A. Govender and R. J. Curry. The "open" hopkinson pressure bar: Towards addressing force equilibrium in specimens with non-uniform deformation. *Journal of Dynamic Behavior of Materials*, 2(1):43–49, 2016.

[69] J.M. Hodgkinson, N.S. Vlachos, J.H. Whitelaw, and J.G. Williams. Drop-weight impact tests with the use of laser-doppler velocimetry. *Proceedings of The Royal Society of London, Series A: Mathematical and Physical Sciences*, 379(1776):133–144, 1982.

[70] T. Fila, I. Kumpova, P. Koudelka, P. Zlamal, D. Vavrik, O. Jirousek, and A. Jung. Dual-energy x-ray micro-ct imaging of hybrid ni/al open-cell foam. *Journal of Instrumentation*, 11(1), 2016.

[71] D. Kytyr, P. Zlamal, P. Koudelka, T. Fila, N. Krcmarova, I. Kumpova, D. Vavrik, A. Gantar, and S. Novak. Deformation analysis of gellan-gum based bone scaffold using on-the-fly tomography. *Materials and Design*, 134:400–417, 2017.

[72] O Jirousek, T Doktor, D Kytyr, P Zlamal, T Fila, P Koudelka, I Jandejsek, and D Vavřík. X-ray and finite element analysis of deformation response of closed-cell metal foam subjected to compressive loading. *Journal of Instrumentation*, 8(02):C02012–C02012, feb 2013.

[73] Roberto Cesareo. Principles and applications of differential tomography. *Nuclear Instruments and Methods in Physics Research Section A: Accelerators, Spectrometers, Detectors and Associated Equipment*, 270(2):572 – 577, 1988.

[74] T. Fila, P. Koudelka, I. Kumpova, M. Vopalensky, J. Sleichrt, V. Rada, P. Zlamal, J. Tarasiuk, and D. Kytyr. Time-lapse micro-CT analysis of fatigue microcrack propagation in cortical bone. *Journal of Instrumentation*, 15(03):C03031, 2020.

[75] P. Koudelka, T. Fila, V. Rada, P. Zlamal, J. Sleichrt, M. Vopalensky, I. Kumpova, P. Benes, D. Vavrik, L. Vavro, M. Vavro, M. Drdacky, and D. Kytyr. In-situ x-ray differential micro-tomography for investigation of water-weakening in quasi-brittle materials subjected to four-point bending. *Materials*, 13(6), 2020.

[76] Philippe Viot, Erwan Plougonven, and Dominique Bernard. Microtomography on polypropylene foam under dynamic loading: 3d analysis of bead morphology evolution. *Composites Part A: Applied Science and Manufacturing*, 39(8):1266 – 1281, 2008. Full-field Measurements in Composites Testing and Analysis.

[77] Isabel Duarte, Matej Vesenjak, and Lovre Krstulovic-Opara. Compressive behaviour of unconstrained and constrained integral-skin closed-cell aluminium foam. *Composite Structures*, 154:231 – 238, 2016.

[78] V.R. Feldgun, Y.S. Karinski, and D.Z. Yankelevsky. A two-phase model to simulate the 1-D shock wave propagation in porous metal foam. *International Journal of Impact Engineering*, 82:113 – 129, 2015. Metallic Foams under Dynamic Loading.

[79] Metal foams. Butterworth-Heinemann, Burlington, 2000.

[80] Isabel Duarte, Matej Vesenjak, and Lovre Krstulovic-Opara. Variation of quasi-static and dynamic compressive properties in single aluminium-alloy foam block. *Procedia Materials Science*, 4:157 – 162, 2014. 8th International Conference on Porous Metals and Metallic Foams.

[81] Joachim Baumeister, Jorg Weise, Eva Hirtz, Klaus Hohne, and Jorg Hohe. Applications of aluminum hybrid foam sandwiches in battery housings for electric vehicles. *Procedia Materials Science*, 4:317 – 321, 2014. 8th International Conference on Porous Metals and Metallic Foams.

[82] Isabel Duarte and John Banhart. A study of aluminium foam formation—kinetics and microstructure. *Acta Materialia*, 48(9):2349–2362, May 2000.

[83] Isabel Duarte, Matej Vesenjak, and Manuel J. Vide. Automated continuous production line of parts made of metallic foams. *Metals*, 9(5):531, May 2019.

[84] F. Baumgartner, I. Duarte, and J. Banhart. Industrialization of powder compact foaming process. *Advanced Engineering Materials*, 2(4):168–174, 2000.

[85] Karsten Stobener and Gerald Rausch. Aluminium foam-polymer composites: Processing and characteristics. *Journal of Materials Science*, 44:1506 – 1511, 2009.

[86] I. Jandejsek, J. Valach, and D. Vavrik. Optimization and calibration of digital image correlation method. In *EAN 2010: 48th International Scientific Conference on Experimental Stress Analysis*, pages 131–136, 2010.

[87] H Kolsky. An investigation of the mechanical properties of materials at very high rates of loading. *Proceedings of the Physical Society. Section B*, 62(11):676–700, 1949.

[88] M. Bussac, P. Collet, G. Gary, and R. Othman. An optimisation method for separating and rebuilding one-dimensional dispersive waves from multi-point measurements. application to elastic or viscoelastic bars. *Journal of the Mechanics and Physics of Solids*, 50(2):321–349, 2002.

[89] H. Zhao and G. Gary. A new method for the separation of waves. application to the shpb technique for an unlimited duration of measurement. *Journal of the Mechanics and Physics of Solids*, 45(7):1185–1202, 1997.

[90] C. Bacon. Separation of waves propagating in an elastic or viscoelastic hopkinson pressure bar with three-dimensional effects. *International Journal of Impact Engineering*, 22(1):55–69, 1999.

[91] L. Wang, K. Labibes, Z. Azari, and G. Pluvinage. Generalization of split hopkinson bar technique to use viscoelastic bars. *International Journal of Impact Engineering*, 15(5):669–686, 1994.

[92] Q. Liu and G. Subhash. Characterization of viscoelastic properties of polymer bar using iterative deconvolution in the time domain. *Mechanics*

Dynamic penetration of cellular solids: Experimental investigation

of Materials, 38(12):1105–1117, 2006.

[93] Michelle S. Hoo Fatt and Dushyanth Sirivolu. A wave propagation model for the high velocity impact response of a composite sandwich panel. *International Journal of Impact Engineering*, 37(2):117 – 130, 2010.

[94] C. Bacon. An experimental method for considering dispersion and attenuation in a viscoelastic hopkinson bar. *Experimental Mechanics*, 38(4):242–249, 1998.

[95] U Ramamurty and A Paul. Variability in mechanical properties of a metal foam. *Acta Materialia*, 52(4):869 – 876, 2004.

```
Jan Sleichrt              - Conceptualization, Investigation, Supervision
Tomas Fila                - Conceptualization, Methodology, Writing - Original
Draft
Petr Koudelka             - Investigation, Writing - Original Draft
Marcel Adorna             - Investigation, Visualization
Jan Falta                 - Investigation, Visualization
Petr Zlamal               - Investigation, Visualization
Jonathan Glinz            - Investigation
Michaela Neuhauserova     - Writing - Original Draft
Tomas Doktor              - Writing - Review & Editing
Anja Mauko                - Resources, Writing - Review & Editing
Daniel Kytyr              - Resources, Writing - Review & Editing
Matej Vesenjak            - Resources, Writing - Review & Editing
Isabel Duarte             - Resources, Writing - Review & Editing
Zoran Ren                 - Resources, Writing - Review & Editing
Ondrej Jirousek           - Writing - Review & Editing
```

Declaration of interests

☒ The authors declare that they have no known competing financial interests or personal relationships that could have appeared to influence the work reported in this paper.

☐The authors declare the following financial interests/personal relationships which may be considered as potential competing interests: